Received: 30 November 2022 | Revised: 7 July 2023 | Accepted: 10 July 2023

DOI: 10.1111/bre.12807

Basin Research IAS EAGE WILEY

RESEARCH ARTICLE

# How displacement analysis may aid fault risking strategies for $CO_2$ storage

**Emma Alexandra Harrower Michie** | **Alvar Braathen**

Department of Geosciences, University of Oslo, Oslo, Norway

**Correspondence**
Emma Alexandra Harrower Michie, Department of Geosciences, University of Oslo, Sem Sælands Vei 1, Oslo 0371, Norway.
Email: emma.michie@liverpool.ac.uk

**Present address**
Emma Alexandra Harrower Michie, Department of Earth, Ocean and Ecological Sciences, School of Environmental Sciences, University of Liverpool, 4 Brownlow Street, Liverpool, L69 3GP, UK

**Funding information**
Norges Forskningsr d; Research Council of Norway, Grant/Award Number: 295061

## Abstract

Developing an accurate understanding of the ways in which faults have grown within a particular region and stratigraphy can aid risk management for $CO_2$ storage sites. Areas of fault interaction lead to differences in the stress field, resulting in an increased strain, which is often accommodated by a high intensity of deformation bands and/or fracturing, dependent on host rock properties. These structures alter the permeability surrounding faults. Hence, detecting areas of interaction of structures throughout the fault growth history allows the identification of locations where high risk may occur in terms of the hydraulic properties of a fault zone. The Vette Fault Zone (VFZ), bounding the Alpha prospect within the potential $CO_2$ Smeaheia storage site, Northern Horda Platform, is shown to have grown from a minimum of seven fault segments. By utilising a comparison with the adjacent Tusse Fault Zone (TFZ), we can identify potential areas of high risk, where fluids may have the ability to flow across or along the VFZ. The high seal strength of the TFZ holding back a large gas column is likely to be created by shale juxtaposition and smearing with cataclastic processes. The same could be assumed for the VFZ, associated with similar tectonics and displaced stratigraphy. However, rather than membrane breaching causing fluids to flow across the fault, potential areas of high risk have been identified at locations of relict breached relay zones, where the initial displacement of the intersecting faults and area of overlap was high. These areas appear to correspond with the location of hydrocarbon contact depth (spill point) along the TFZ. Using the same assumptions for the VFZ, we can observe one potential area of high risk, which lies within the area of suggested $CO_2$ accumulation.

KEYWORDS

$CO_2$ storage, fault growth, fault seal, risk assessment, Smeaheia

## 1 | INTRODUCTION

Known depleted oil fields or aquifers within the subsurface have been proposed, and exploited, for $CO_2$ storage. Carbon capture and storage solutions are required to reduce emissions of greenhouse gases in order to reach the 2°C goal of the Paris Agreement (e.g. Birol, 2008; Rogelj et al., 2016). This study focuses on one candidate for $CO_2$ storage within the Northern Horda Platform, Norwegian North Sea, known as the Smeaheia site (Lauritsen et al., 2018; Mulrooney et al., 2020; Osmond et al., 2022; Sundal et al., 2014; Wu et al., 2021). The Alpha prospect within this storage site is bound by a large, deep-seated basement fault known as the Vette Fault Zone (VFZ) (Mulrooney et al., 2020), with the storage unit being a clean sand with high porosity and permeability, known as the Sognefjord Formation. Faults pose an important challenge, where accurately predicting the sealing potential and any reactivation potential, is crucial to retain any $CO_2$. Traditional methods of fault seal prediction, such as the shale gouge ratio (SGR), are generally used for oil and gas accumulation estimates, predicting the column height that can be retained by the bounding faults (Bretan et al., 2003; Fisher & Knipe, 1998; Sperrevik et al., 2002; Yielding et al., 1997, 2010). While these are tried and tested methods, uncertainties remain, such as the wettability of the $CO_2$-brine-rock system (i.e. the interfacial tension and contact angle; Karolytė et al., 2020), the subseismic-scale resolution of irregularities to fault core formation, and any damage surrounding faults that may enhance or reduce fluid flow. This contribution focuses on the latter two uncertainties. These uncertainties are potentially detrimental to the $CO_2$ storage capacity, when the prospect is bound by a fault. Hence, understanding and reducing any uncertainties to fault seal, such as predicting the variation in deformation along fault strike associated with fault growth, that may act to alter the hydraulic behaviour of a fault, is crucial when assessing any storage site.

The conceptual displacement model for isolated faults is generally an elliptical shape, whereby displacement is greatest in the centre of the fault, decreasing gradually towards the tip (e.g. Barnett et al., 1987; Nicol et al., 1996; Peacock & Sanderson, 1991; Rippon, 1984; Walsh & Watterson, 1988, 1991). During fault growth, isolated faults can connect vertically and/or laterally, initially starting as soft-linked relay zones where the displacement maxima are not significantly influenced by the linkage (Morley et al., 1990; Peacock & Sanderson, 1991). These soft-linked structures can become hard-linked, where a common displacement maxima will then occur along the length of the connected fault as it accumulates displacement. This continues through fault evolution and can lead to fault zones where these relict relay zones are no longer obvious in map view but can be identified through subtle variations in displacement along fault strike and down fault dip (e.g. Serck & Braathen, 2019). Case studies show that throw minima reflecting segment linkage remain despite significant fault offset after linkage (Serck & Braathen, 2019; Torabi et al., 2019). For this analysis, throw–distance (T-D) plots are created through detailed seismic interpretation of the subsurface, and used to identify fault segment linkage, often interpreted at areas of displacement lows (e.g. Cartwright et al., 1996). For accuracy during this analysis, it is important to take into consideration continuous deformation by ductile strains (e.g. folding), which can contribute to local throw minima (Jackson et al., 2017, 2017b; Walsh et al., 1996).

Intersecting fault segments have been shown to alter their hydraulic behaviour along fault strike. Specifically, soft-linked relay zones are often inferred as acting as a conduit, increasing fluid flow connectivity at either side of the fault (e.g. Bense & Van Balen, 2004; Childs et al., 1995; Fossen & Rotevatn, 2016; Peacock & Sanderson, 1994; Rotevatn et al., 2009; Trudgill & Cartwright, 1994). A high intensity of deformation bands has also been recorded at relay zones (e.g. Peacock & Sanderson, 1994; Rotevatn et al., 2007; Shipton et al., 2005), which can alter the hydraulic behaviour of the faults once these relay zones become hard-linked. Hence, accurately assessing how the faults have grown, and locating where relict breached relays occur, may prove to be crucial when considering across- or up-fault fluid flow for the assessment of any fault-bound $CO_2$ storage site.

In order to assess any possible locations of high risk along fault strike, that is at areas of relict breached relays, we need to understand which fault growth model(s) may best describe the studied faults. Two main fault growth models have been described: propagating fault model (e.g. Cartwright et al., 1995; Cowie & Scholz, 1992a, 1992b; Dawers & Anders, 1995; Huggins et al., 1995; Jackson & Rotevatn, 2013; Rotevatn et al., 2019; Walsh & Watterson, 1988; Walsh et al., 2003) and the constant-length

### Highlights

- Detailed fault seal analysis has been performed, identifying mechanisms other than gouge or smear for fault leakage.
- Areas of high risk are assessed in terms of fault growth history.
- Fault growth history for the studied faults follow the constant-length model.
- Relict fault-fault intersections showing high amplitude / wavelength overlaps are identified as areas of high risk.

fault model (Childs et al., 1995; Cowie, 1998; Jackson & Rotevatn, 2013; Jackson et al., 2017; Morley et al., 1990; Nicol et al., 2005, 2010, 2020; Rotevatn et al., 2018, 2019; Walsh et al., 2002, 2003). The propagating fault model can be divided into non-coherent or coherent faults (Childs et al., 2017): for non-coherent faults, this model describes unconnected segments that are all aligned in a similar trend but not kinematically related, whereas for coherent faults, the model describes individual faults that form a single larger structure but are not geometrically connected. In both scenarios, the fault propagates as the displacement increases. For non-coherent faults, the faults link-up laterally with time, and for coherent faults, new segments can form at the tip. Conversely, the constant-length model describes a fault that has established its final length early in its evolution, where relay formation and breaching occurred rapidly, after which, fault growth occurs through cumulative displacement increase (Childs et al., 2017). In this scenario, fault propagation occurs only through linkage between segments. While these are the two widely accepted end-member models for fault growth, a hybrid of these behaviours has recently been suggested as an alternative (Rotevatn et al., 2019). Identifying the model that best describes a fault's growth history is often performed by utilising T-D plots, combined with displacement backstripping, and integration with growth strata, specifically through expansion index analysis (Cartwright et al., 1998; Jackson et al., 2017; Lewis et al., 2013; Thorsen, 1963).

Not only is it important to locate these relict breached relays that have occurred throughout fault growth history, through methods such as T-D plots, it is also crucial to be able to predict how, and to what extent, they may influence the sealing potential of a fault zone. Through this contribution, we aim to accurately assess the fault growth model that best describes the large prospect-bounding faults within the study area and analyse areas of relict breached relay zones to assess how they may influence the overall sealing potential of these faults.

## 2 | STUDY AREA

A potential $CO_2$ storage site known as Smeaheia (Halland et al., 2011; Lauritsen et al., 2018; Mulrooney et al., 2020; Statoil, 2016) has been proposed, associated with the prospect well 32/4–1 originally drilled for exploration purposes (Goldsmith, 2000). However, well data from 32/4–1 recorded no oil shows (32/4–1 T2 Final Well report 1997). Hence, this site has been assessed for the potential for $CO_2$ storage within a saline aquifer. The Smeaheia site is located within the Northern Horda Platform, approximately 40 km Northwest of the Kollsnes processing plant, and roughly 20 km directly East of Troll East (Figure 1). The Northern Horda Platform is a 300 km by 100 km, N-S elongated structural high located along the eastern margin of the northern North Sea (Duffy et al., 2015; Færseth, 1996; Mulrooney et al., 2020; Osmond et al., 2022; Whipp et al., 2014; Figures 1 and 2). The Horda Platform contains several half-graben bounding fault systems associated with deep-seated, west-dipping basement faults that are observed to displace km-scale strata (Badley et al., 1988; Bell et al., 2014; Færseth, 1996; Whipp et al., 2014; Yielding et al., 1991).

Two of the deep-seated basement faults within the Horda Platform bound the potential Smeaheia $CO_2$ storage site: the VFZ, bounding the Alpha prospect, and the Øygarden Fault Complex, bounding the Beta prospect (Figures 1 and 2). These are thick-skinned faults that bound an east-tilting half graben. For this study, we focus only on the Alpha prospect, which is a 3-way closure bound by the VFZ (Figure 1). The VFZ is observed as the next thick-skinned fault adjacent directly to the east of the Tusse Fault Zone (TFZ); a half-graben bounding, sealing fault allowing for the accumulation of significant hydrocarbon column in Troll East. The VFZ follows a roughly north–south trend, showing several complexities, such as relay zones, along its length (Mulrooney et al., 2020).

Several smaller-scale, thin-skinned northwest-southeast-striking faults are also recorded within the Smeaheia site (Mulrooney et al., 2020) and within the adjacent Troll Field. These faults are associated with the Jurassic to Cretaceous rifting event that also caused reactivation of the Permo-Triassic basement-seated faults (Deng et al., 2017; Færseth et al., 1995); they only affect post-Upper Triassic stratigraphy. Low throws (<100 m) are recorded for these thin-skinned faults. These faults are occasionally observed to intersect the larger half-graben bounding faults (VFZ and TFZ), affecting the overall throw profiles, but more often than not these do not show any throw partitioning with the larger thick-skinned faults.

The main storage formation that is the focus of this study is the Middle-Upper Jurassic Sognefjord Formation of the Viking Group. The Sognefjord Formation is a saline aquifer within Smeaheia, and is composed of coastal to shallow marine sandstones (Dreyer et al., 2005; Holgate et al., 2013; Patruno et al., 2015). It occurs at approximately 1200 m depth at the Alpha prospect and has been recorded as having a permeability of 440–4000 mD and a porosity of 30–39% (Mondol et al., 2018; Ringrose et al., 2017; Statoil, 2016). It has a top and lateral seal from deep marine, organic-rich mudstones of the Draupne Formation, along with deep water marl, carbonates and shaley units in the Cromer Knoll and Shetland Groups above the Base Cretaceous Unconformity (Gradstein & Waters, 2016; Isaksen & Ledje, 2001; Justwan & Dahl, 2005; Nybakken & Bäckstrøm, 1989).

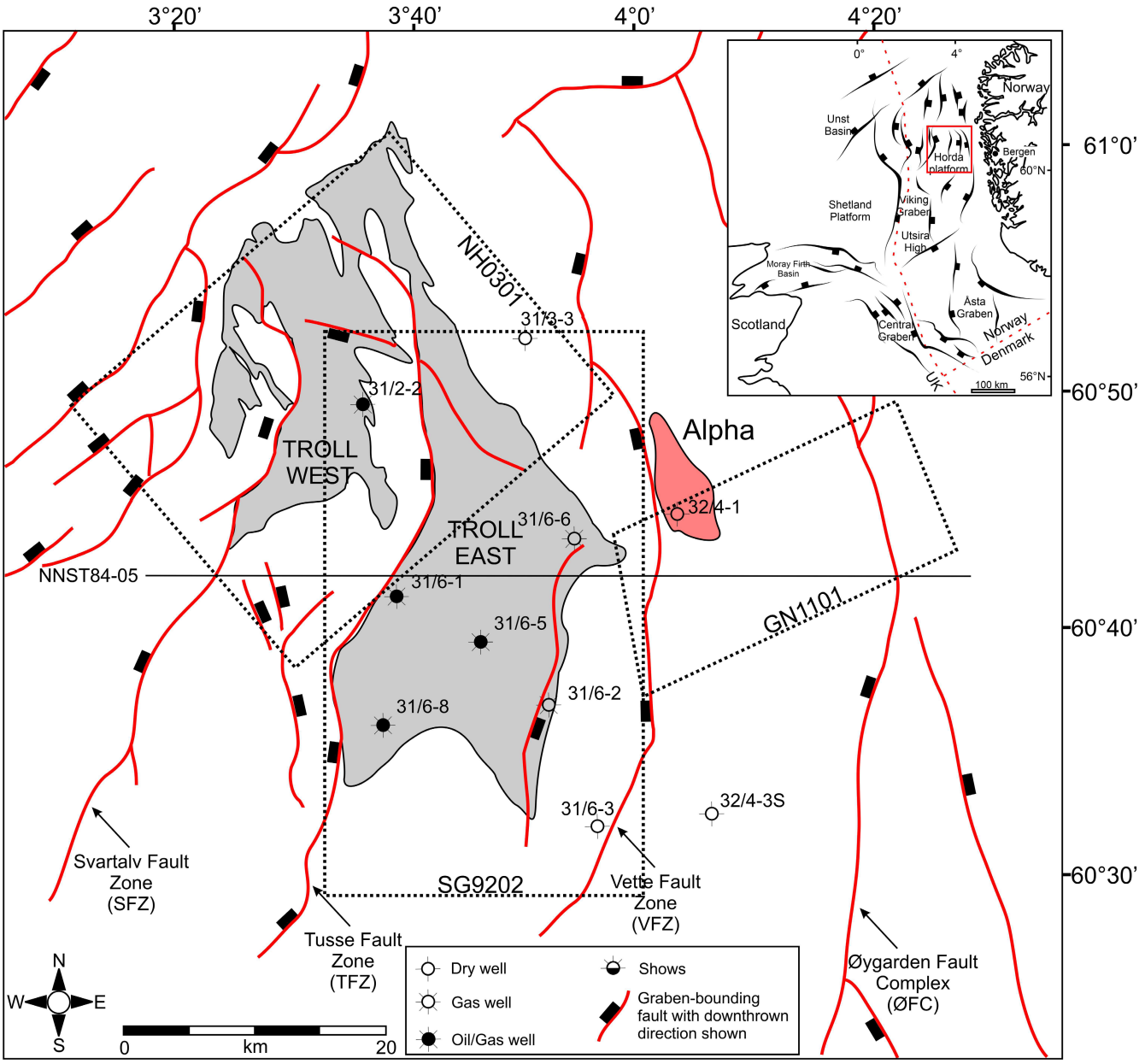


**FIGURE 1** Location of the Smeaheia site within the Northern Horda Platform, showing the Alpha prospect by the red outline. Location of Troll East and West fields shown by the grey outline. Main faults shown by the red lines. Location and extents of each 3D survey used is also shown. Wells used within this analysis shown. Location of 2D seismic line NNST84-05 showing regional cross section of the area on Figure 2 shown. From Norwegian Petroleum Directorate Fact Maps (http://factmaps.npd.no/factmaps/3_0/). Inset: Location of the Horda platform in relation to the North Sea, Norwegian and Scottish coastline, after Mulrooney et al. (2020). Main structural elements, such as basin-bounding faults, main basins and structural highs, shown.

## 3 | METHODOLOGY

Subsurface interpretation has been performed using three main 3D surveys: GN1101, SG9202 and NH0301 (Figure 2). A total of five seismic horizons have been interpreted: top Shetland Group, top Cromer Knoll Group, top Draupne Formation, top Sognefjord Formation and top Brent Group. The VFZ has been interpreted using the GN1101 survey. However, it is important to note that this survey does not extend far enough to the north and south to interpret the entire fault structure. Hence, only the portion of fault that is observed on GN1101 survey has been analysed. The TFZ has been interpreted using surveys SG9202 and NH0301. Both the VFZ and TFZ follow the same trend: roughly north–south and displace the same stratigraphy. Hence, general lessons learnt from the TFZ bounding the well-known Troll East Field may also be applicable to the adjacent VFZ.

All 3D surveys are time-migrated data sets that have subsequently been depth converted using a velocity model

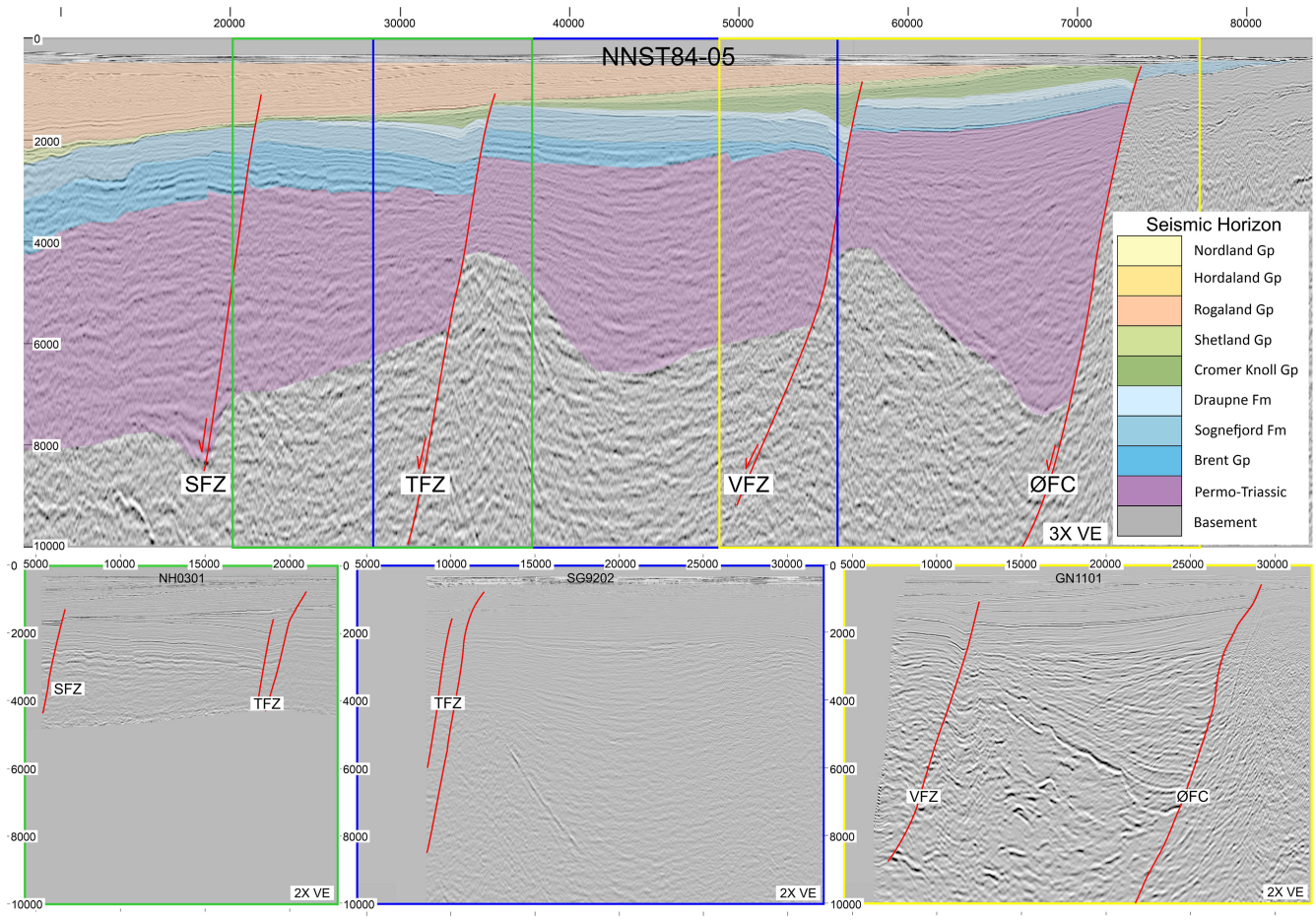


**FIGURE 2** Regional cross section from 2D seismic line NNST84-05 showing the location and nature of the main half-graben bounding faults: Svartalv Fault Zone (SVZ), Tusse Fault Zone (TFZ), Vette Fault Zone (VFZ) and the Øygarden Fault Complex (ØFC), along with the varying stratigraphy within the area (location of seismic section shown on Figure 1). Location of the 3 3D surveys used within this analysis shown: yellow box (GN1101), blue box (SG9202) and green box (NH0301). Seismic lines from each of the 3D surveys intersecting the 2D seismic line is shown, along with the location and nature of the main half-graben bounding faults.

that has been created using quality controlled (QC) two way time (TWT) curves from 15 wells from the Troll and Smeaheia areas: 31/2–1, 31/2-2R, 31/2-4R, 31/2–5, 31/2–8, 31/3–1, 31/3–3, 31/5–2, 31/6–1, 31/6-2R, 31/6–3, 31/6–6, 32/2–1, 32/4–1T2 and 32/4–3S. Other wells in the area have no velocity data. All three seismic surveys show good seismic resolution. Using frequency and interval velocity, the resolution at the Sognefjord level is roughly 15.75 m on the GN1101 survey, 13.1 m on the NH0301 survey and 12.1 m on the SG9202, suitable for detailed structural interpretation. However, due to differences in processing, the resulting reflectivity and contrast varies between each survey. Higher reflectivity and contrast occur for the GN1101 and NH0301 surveys, and hence show a good seismic image quality. However, lower reflectivity and contrast is observed for the SG9202 survey, resulting in lower image quality (Figure 2).

Survey GN1101 was shot in 2011 by Gassnova SF, with an inline spacing of 25 m and a crossline spacing of 12.5 m, covering an area of 442.25 km$^2$. Crosslines are oriented 065°, and inlines are oriented 155°. Survey NH0301 was shot in 2003 by Norsk Hydro ASA with an inline spacing of 18.75 m and a crossline spacing of 12.5 m, covering an area of 715 km$^2$. Crosslines are oriented 048.9° and inlines are oriented 318.9°. Survey SG9202 was shot in 1992 by Saga Petroleum ASA, with an inline and crossline spacing of 12.5 m, covering an area of 880 km$^2$. Crosslines are orientated 0°, and inlines are 090°. GN1101 and NH0301 have normal polarity, whereas SG9202 shows reverse polarity. All seismic surveys show a zero-phase wavelet.

An optimum fault picking strategy has been identified (Michie et al., 2021, 2022) and has been utilised for the interpretation of the TFZ and the VFZ. Specifically, the sizeable half-graben bounding faults that extend for several kilometres require a picking strategy that best captures all detail, but not too high resolution to generate irregular fault surfaces that are not an accurate representation of the faults due to human (Faleide et al., 2021) and triangulation errors. To this end, the fault picking strategy used

within this study is to pick fault segments at a spacing of 100 m. Rigorous quality control has been performed to maintain continuity between interpreted lines.

The fault surfaces have been created using unconstrained triangulation. Unconstrained triangulation generates a fault surface that honours all data points but allows the triangulation of fault segments without forcing the surface to conform to the lines between adjacent points on the same segment. Note that no additional smoothing has been applied to the modelled fault surfaces. Fault attributes such as strike, dip, throw, are calculated and mapped onto the fault surfaces at a resolution of 8 m lateral by 4 m vertical, providing an optimum resolution at the seismic scale without the need to extend processing time for a finer resolution.

Fault cut-offs (intersection lines between horizon and fault) have been picked on both the VFZ and TFZ, for the 5 mapped seismic horizons. The fault cut-offs have been picked using a combination of seismic slicing, at a distance of 10 m from the fault to remove any seismic noise, and utilising intersecting lines that are roughly perpendicular to the fault trace, at a spacing of 100 m. The spacing of 100 m for fault cut-off modelling has been chosen as this has been shown to incorporate all detail that is also observed when using a narrower line spacing (Michie et al., 2021). Complications arise when picking fault cut-offs due to significant drag occurring in the hanging wall. Fault cut-offs have been picked in two ways: (i) honouring the drag, in order to accurately capture the juxtapositions for fault seal analysis, and (ii) ignoring the drag, in order to accurately interpret fault growth. These fault cut-offs are used to calculate fault throw, which is displayed as both throw–distance (T-D) plots and mapped onto the 3D fault surfaces, and are used to analyse fault displacement and growth. Areas where fault throw has significantly changed from the background trend (i.e. roughly >50 m) are identified as areas of relict breached relay zones. This allows for the analysis of the location of relict breached relays, where faults once intersected. Splay faults also can cause such irregularity to the T-D plots, and hence these are eliminated from this analysis. The fault cut-offs are also used to drape the well-derived VShale curve onto the fault surfaces to calculate the shale gouge ratio (SGR) when used in combination with the calculated throw, for fault seal analysis.

## 3.1 | Fault growth analysis

In order to accurately assess the most relevant model that best describes the way in which a fault has grown, we have utilised a number of methodologies. Specifically, we have produced T-D plots, as described above, to identify areas where segmentation was likely to occur. These T-D plots have been generated using fault cut-offs that do not incorporate folding, accounting for ductile strain that may adjust for extension-induced deformation (Jackson et al., 2017; Walsh et al., 1996).

Fault segmentation is often interpreted at sudden changes in fault throw (i.e. roughly >50 m, where the throw irregularity is unlikely to be a product of picking error or resolution issues), and where these displacement lows cannot be attributed to any other mechanism such as intersecting splay faults (e.g. Cartwright et al., 1996; Serck & Braathen, 2019; Torabi et al., 2019). Although T-D plots alone cannot show the precise fault growth model, they can highlight areas of potential relict breached relays, identifying areas of potential high risk in terms of $CO_2$ storage.

Analysis has been done on both the VFZ and the TFZ. The use of the TFZ data aids the analysis of fault growth and how areas of previous fault intersection may impact fluid flow across or up the fault, for example at areas identified as relict breached relays. The TFZ is a known barrier to fluid flow, allowing for the accumulation of hydrocarbon in Troll East. Hence, any identified complexities in the fault structure due to fault growth processes can be assessed in terms of likely impact on the sealing potential of the fault.

### 3.1.1 | Expansion index plots

Complementary analysis to T-D plots has also been performed, to understand the fault growth history. Specifically, Expansion Index (EI) plots have been produced for the 5 key horizons (Brent Gp, Sognefjord Fm, Draupne Fm, Cromer Knoll Gp and Shetland Gp) along the length of a fault to assess whether a fault grew by a constant-length or propagating fault model. Since the oldest horizon picked is the top of the Brent Gp, this analysis will only provide information pertaining to later stage fault growth stages from the Brent Gp onwards, specifically focusing on the reactivation within the Late Jurassic. This method provides no data or analysis for the initial Permo-Triassic fault stage. EI plots have been generated by dividing the hanging wall (HW) thickness of a specific stratal unit by its corresponding footwall (FW) thickness and plotting against geological time. These have then been plotted against the depth at which these stratal units occur (Cartwright et al., 1998; Jackson & Rotevatn, 2013; Thorsen, 1963). EI plots have been created at the fault tip, mid-point and maximum throw along the fault, to show how the fault has grown. Further, EI has been plotted along the length of both the VFZ and the TFZ, with EI values generated at a constant spacing of 1 km. Note that the base Brent Gp horizon has not been mapped in 3D but is simply observed and used to measure FW and

HW thickness on these 2D seismic sections for means of EI calculations.

EI values of 1 suggest that no syn-depositional fault activity occurred, while EI values of >1 indicate that across-fault thickening and syn-depositional fault activity occurred (Cartwright et al., 1998; Thorsen, 1963). EI plots provide information regarding the 1D evolution of these faults (Cartwright et al., 1998; Jackson & Rotevatn, 2013; Thorsen, 1963), as well as providing an understanding of the correct model of fault propagation (Jackson et al., 2017). Specifically, utilising the EI plots along fault strike can indicate the location of fault tips at certain time intervals, and hence may be used to distinguish whether the fault grew by the constant-length or the propagating fault model. If EI values of >1 are identified at, or close to the current fault tip for older stratal units, this information could be used to interpret a fault that has grown by the constant-length model. Conversely, if the older stratal units show EI values of >1 only within the inner portions of the current fault location, this could indicate the fault has grown by the propagating fault model (Jackson et al., 2017).

It is important to note, however, that simple EI analysis assumes that all accommodation space is occupied by the successive layers of sediment. However, EI may simply reflect a change in sedimentation style (Bertram & Milton, 1988). For example, there may be a period of the basin being sediment-starved during active extension, after which passive infill occurred during a phase of relative tectonic quiescence, as mentioned in Roberts et al. (2019).

### 3.1.2 | Displacement backstripping

Displacement backstripping has been performed to aid with analysis of which fault growth model is most appropriate for a specific seismic-scale segmented normal fault array. Since these faults are syn-sedimentary, we utilise the 'original' backstripping method (cf. Jackson et al., 2017). The original backstripping method subtracts the throw measured across a shallower horizon from throw measured across a deeper horizon at the same along-strike position. This process is then repeated for successively deeper horizons (Chapman & Meneilly, 1991; Petersen et al., 1992). For these types of analyses, ductile strain may account for considerable amount of extension-induced deformation (Jackson et al., 2017; Walsh et al., 1996). Hence, we have accounted for the ductile strains, which in these examples manifests itself as folding. It is important to note, however, that the VFZ only penetrates the Top Cromer Knoll Group, Top Shetland Group and Top Rogaland Formation within the northern half of this fault. Hence, there are limited mapped horizons that span the entirety of the VFZ that have been used for this analysis, and these periods of fault growth will go unresolved for this method of analysis. Utilising both T-D plots and EI plots will help to fill this gap. Furthermore, it is important to note that, similar to EI analysis, displacement backstripping only provides information regarding fault growth from the Brent Gp onwards through fault reactivation in the Late Jurassic, with no information regarding the initial Permo-Triassic faulting, due to poor resolution of the basement strata resulting in a high degree of uncertainty regarding fault–horizon intersections.

## 3.2 | Fault seal analysis

As a complimentary method to fully understand how the faults may influence the fluid flow potential, we have performed fault seal analysis. Specifically, we have examined the juxtaposition diagrams (Allan, 1989) and calculated the shale gouge ratio (SGR) (Yielding et al., 1997) on the VFZ and TFZ. While the sealing potential is simply predicted for the VFZ, the fault seal potential for the TFZ can be calibrated with the recorded hydrocarbons in place, in order to assess whether fault seal plays a crucial role in dictating the hydrocarbon contact depth.

One nearby well has been used for fault seal analysis of the VFZ: 31/6–6. This well is within the immediate HW of the VFZ (Figures 1 and 3), and has been chosen as it has a well-constrained gamma ray (GR) log throughout the entire succession, with no other wells existing within the FW of the VFZ (at or near the Alpha prospect) that contain a complete GR curve. Six wells have been used for fault seal analysis of the TFZ: 31/2–2, 31/3–3, 31/6–1, 31/6–2, 31/6–5, 31/6–6 and 31/6–8 (Figures 1 and 3). These wells were chosen as the GR logs cover a large portion of the stratigraphy throughout deep well trajectories, with values that showed little/no significant irregular spikes. Furthermore, these provide clay content information from both the HW and the FW along the length of the fault, and from wells that penetrate the relevant stratigraphic intervals. Note, however, that none of the GR logs have been quality controlled (QC), and hence may lead to high uncertainty in the resulting SGR values. For example, no analysis has been performed correlating the GR with the corresponding cuttings examined by X-ray diffraction (XRD) providing information on the clay content. Instead, a simple linear transform has been performed to convert the GR log into a VShale log in order to perform the fault seal analysis. Specifically, 100% VShale has been assigned to the maximum average GR value and 0% VShale has been assigned to the minimum average GR value, with a linear relationship between these being assumed (e.g. Lyon et al., 2005; Rider, 2000). Note that different minimum and maximum

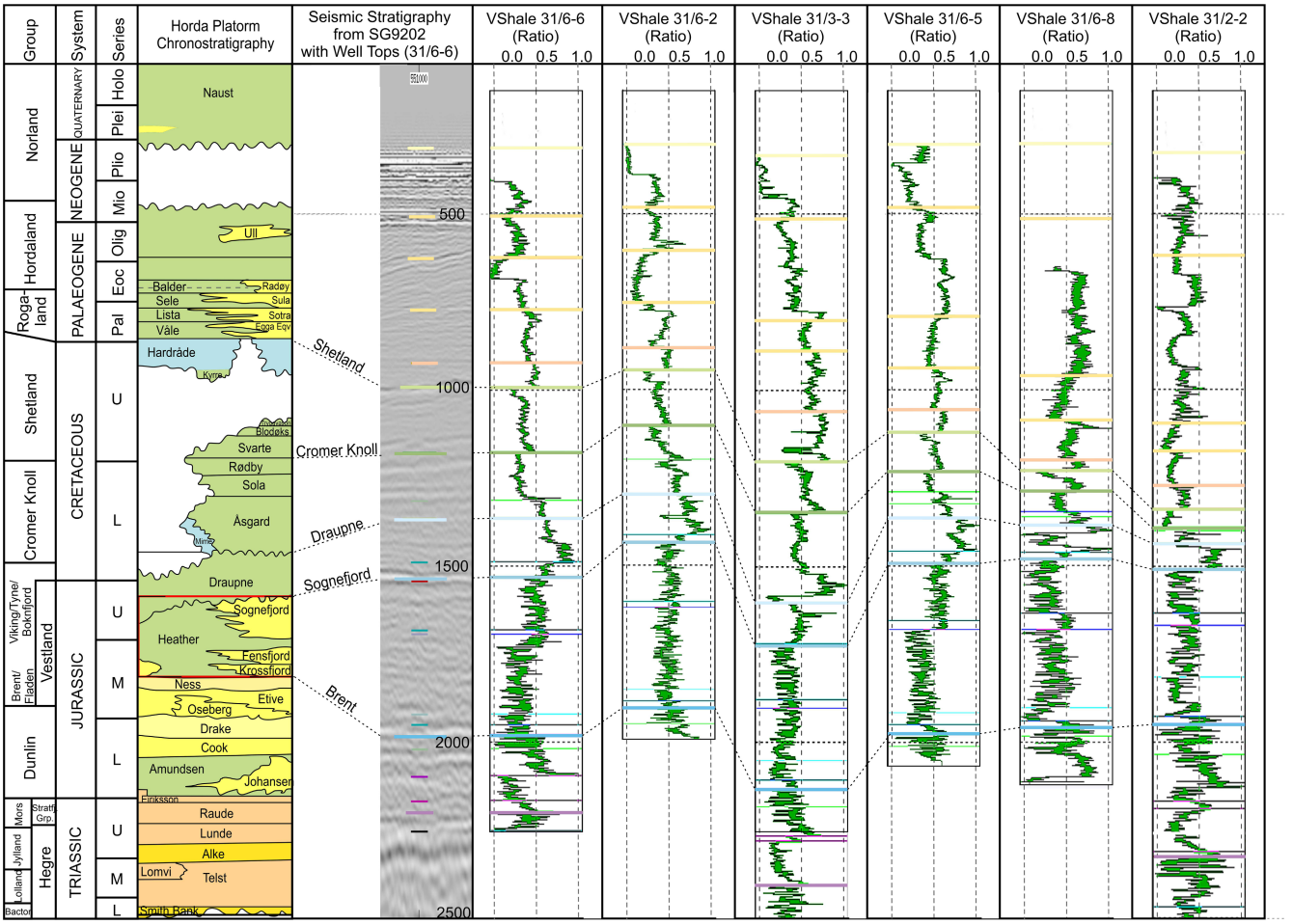


**FIGURE 3** Lithostratigraphic chart of the Horda Platform from Halland et al. (2011). The main primary horizons used within this analysis are shown in the seismic stratigraphic framework section, from intersecting well 31/6–6 within the survey SG9202. Marker horizons shown, corresponding to the lithostratigraphic column. VShale curves from well 31/6–6, 31/6–2, 31/3–3, 31/6–5, 31/6–8, 31/2–2 shown (from East to West), with marker horizons for reference.

GR values have been used for each well. Since a high uncertainty occurs with the resulting SGR values, this provides a simple first pass analysis of whether the fault may act as a seal and where along the fault a seep point is likely to occur. The VShale is draped onto the fault using the locations of picked fault cut-offs, which tie with well picks. The VShale has been used to locate areas where low VShale (<0.4) overlaps may occur, that is at sand–sand juxtapositions, as well as to calculate the SGR at these sand–sand locations. The SGR is calculated using the equation from Yielding et al. (1997):

$$\mathrm{SGR} = \frac{\sum(\mathrm{Vcl} \times \Delta z)}{\text{Fault throw}} \times 100\,\% \tag{1}$$

where the Vcl is the clay volume fraction in the fault zone, and $\Delta z$ is the thickness of each reservoir zone (Yielding et al., 1997). A high SGR predicts that seep across the fault is unlikely.

For a continued analysis, the SGR has been used to estimate a maximum hydrocarbon column height. Since the VFZ is a bounding fault for a potential $CO_2$ storage site, this analysis has only been done for the TFZ, using the known density for the gas within Troll East. The density of the gas leg is taken as 122 kg/m3, based on drilling tests from well 31/6–1 (https://factpages.npd.no/en/wellbore/pageview/exploration/all/22). The density of the water leg has been measured as 1010 kg/m3 from well 31/6–1 (https://factpages.npd.no/en/wellbore/pageview/exploration/all/22). Location of well 31/6–1 can be observed on Figure 1. The algorithm outlined by Yielding et al. (2010) has been used for this analysis, whereby the maximum column height is given as:

$$\Delta P = 0.175 \times \mathrm{SGR} - 3.5 \tag{2}$$

where $\Delta P$ is the buoyancy force in bars. This analysis has been done in order to assess where the shallowest leak point may be within the Troll East gas Field; whether the fault would be able to retain enough hydrocarbons to fill to spill, or whether an area along the fault will act as a leak point.

# 4 | RESULTS

## 4.1 | Fault growth history

### 4.1.1 | T-D plots

The throw profiles for both the VFZ and TFZ show an overall maximum throw dissipating towards the fault tips, as would generally be expected (e.g. Nicol et al., 1996; Peacock & Sanderson, 1991; Walsh & Watterson, 1988, 1991; Figure 4). However, some significant variations are also observed along the length of both faults. These variations can be partly attributed to current splay faults (in the FW of the both the VFZ and TFZ, and in the HW of the TFZ), but can also be due to relict breached relay zones, where minor faulting has subsequently joined together at fault intersections throughout the growth history. These areas of relict breached relay zones are better observed using throw–distance (T-D) plots rather than throw profiles displayed on fault surfaces (Figures 4 vs. 5). Hence, top Sognefjord T-D plots have been utilised to analyse fault growth, and interpreting areas where relict breached relay zones may have occurred.

For the area that the VFZ is observed using the survey GN1101, we can interpret six areas of relict breached relay zones using T-D plots, corresponding to seven initial fault segments that have subsequently grown together to create this single portion of the VFZ surface (Figure 5b). These initially fault segments often correspond with observed low amplitude transverse fault folds, where the transverse synclines and anticlines reflect displacement maxima near the centre of fault segments and displacement minima near fault tips, respectively (cf. Schlische, 1995; Serck &

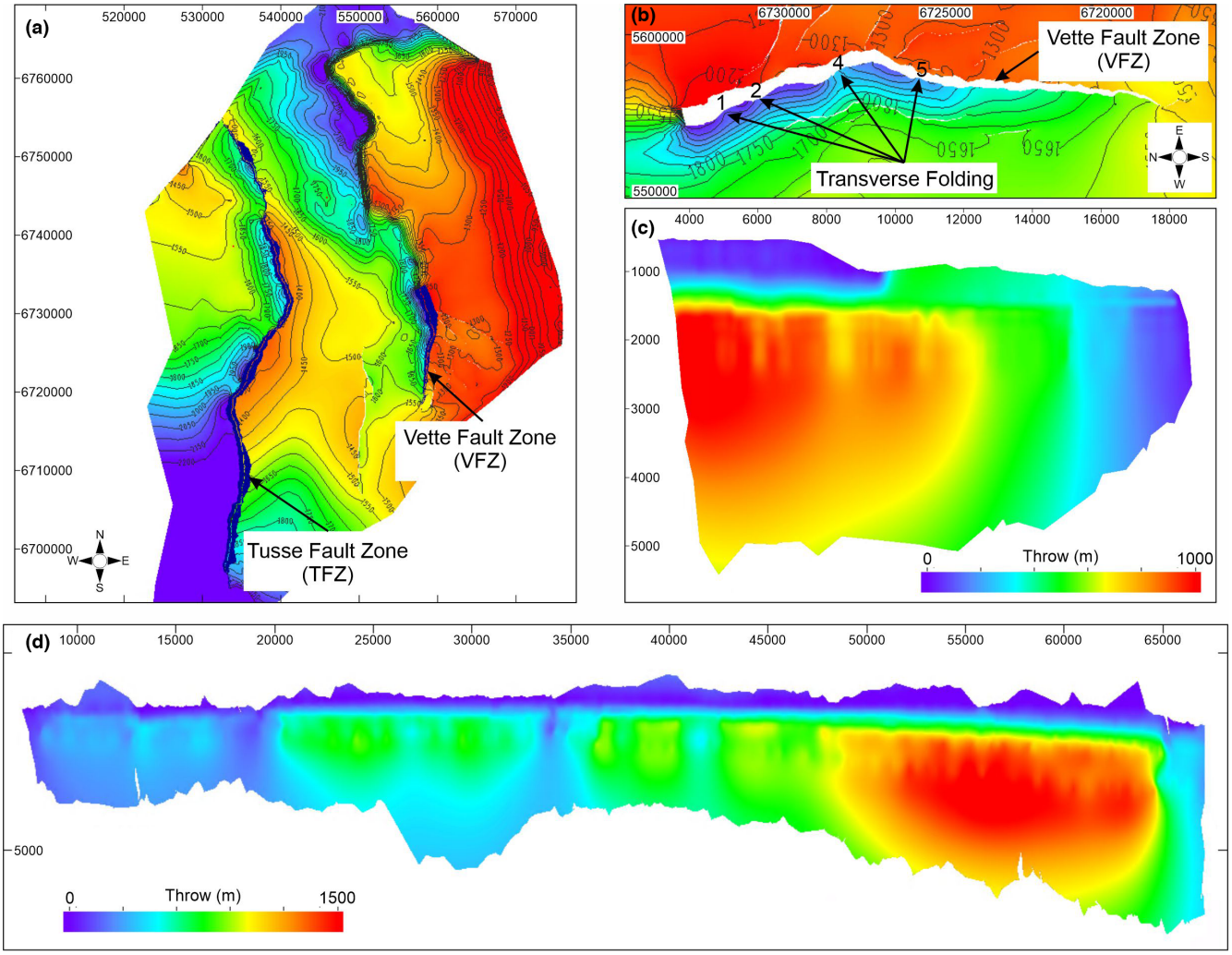


FIGURE 4 (a) Depth structure map of the Top Sognefjord Formation. (b) Depth structure map of the top Sognefjord Formation surrounding the Vette Fault Zone (VFZ), showing the fault heave and transverse folding that occurs within the hanging wall of the VFZ. Numbers next to transverse folding arrows correspond to intersections numbered on Figure 5b. (c) Fault throw displayed along fault strike of the VFZ. N to left, depth in metres on left axis. (d) Fault throw displayed along fault strike of the Tusse Fault Zone (TFZ). N to left, depth in metres on left axis. The fault throws show an overall a high displacement that dissipates towards the fault tips for both faults; however, some variations about this overall trend are observed along-strike.

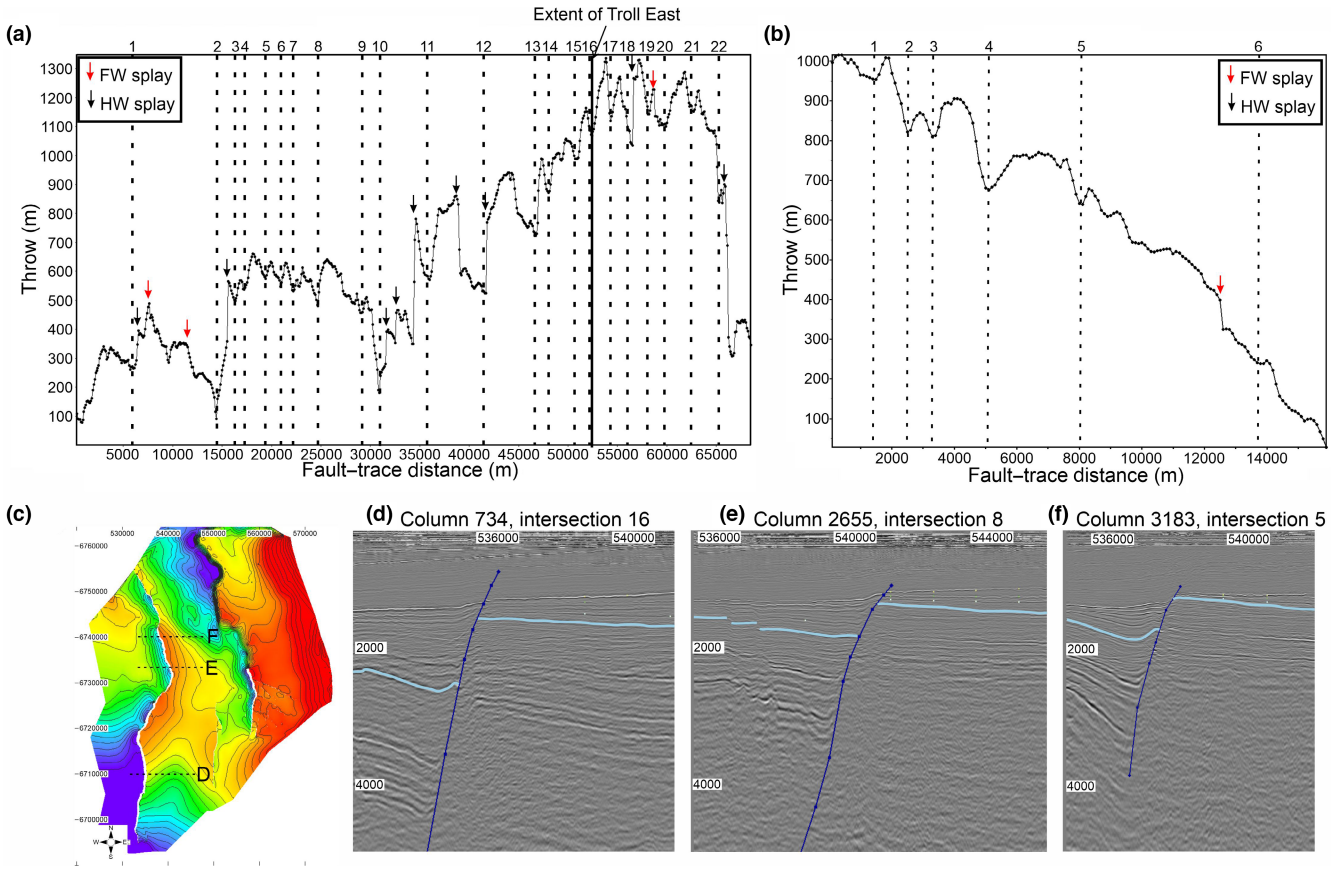


**FIGURE 5** Throw–distance (T-D) plots of the Top Sognefjord horizon for the Tusse Fault Zone (TFZ) (a) and Vette Fault Zone (VFZ) (b). Location of Footwall (FW) and Hanging wall (HW) splays shown by red and black arrows, respectively. Location of interpreted breached relay zones shown as vertical dashed lines and labelled with numbers. The southern extent of Troll East hydrocarbon accumulation shown on figure (a). 22 interpreted breached relay zones are observed for the TFZ and 7 interpreted breached relay zones are observed along the VFZ. Note that the distribution and geometry of these intersections vary along both faults. (c) Map of the Sognefjord Formation showing the location of seismic sections shown in Figures (d–f), all from seismic survey SG9202. (d) Seismic section column 734, intersecting the location where the potential spill point is located, and where an interpreted large relict breach relay zone occurs; amplitude/wavelength 0.2. (e) Seismic section column 2655, showing a moderate sized relict breached relay zone; amplitude/wavelength 0.12. (f) Seismic section column 3183 showing a small sized relict breached relay zone; amplitude/wavelength 0.075. See Figure 10 for definition of amplitude/wavelength. Top Sognefjord shown in blue on all seismic lines, (d–f).

Braathen, 2019; Figure 4b). Note that not all interpreted relict breached relay zones correspond with transverse fault folds, particularly at areas where the throw gradient at these fault intersections is relatively low. The seven fault segments are not observed to be distributed evenly along its length, and the size of the overlaps vary considerably, suggesting varying sizes of the initial fault segments within the overall fault array. Towards the northern end of the VFZ, the areas of interpreted relict breached relay zones are closer spaced, indicating that the initial fault segments are shorter in length. However, at roughly 8000 m from the north, the relay zones are shown roughly 5750 m apart, suggesting longer initial fault segments. Furthermore, the amplitude of the intersections (i.e. the size of the throw overlap) is lower in the southern portion of the VFZ.

TD plots for the TFZ show 22 areas of relict breached relay zones, corresponding to 23 initial fault segments that have subsequently grown together (Figure 5a). Similar to the VFZ, these 23 fault segments are not evenly distributed along its length, and their geometry (i.e. size and amplitude) is observed to vary. The northern 15 km is interpreted to only have two fault segments. From 15 km to 25 km from the north, the interpreted relict breached relay zones are observed in close proximity, after which the spacing increases until roughly 45.5 km. From 45.5 km until 65 km from the north, the spacing of these potential relict breached relays is again observed to decrease (Figure 5a). Note that there are no discernable features observed on the seismic sections at any interpreted relict breached relay zones, regardless of their size (Figure 5c–f); whether the overlap area and throw amplitude of the relict breach relay zone is measured as being relatively small (Figure 5f) or relatively large (Figure 5d).

As mentioned previously, not only do the relict fault segments cause variations in the T-D plots, so do intersecting

HW and FW splay faults. However, the majority of subsidiary faults within the FW do not intersect the VFZ, but die out very close to the fault and are shown to have no influence on the throw of the VFZ. Here, we can only see 1 intersecting FW fault, with no intersecting HW splays (Figure 5b). Similarly, the TFZ has only 3 intersecting FW splays along its entire length (Figure 5a, red arrows). Conversely, the TFZ shows several (9) HW splays (Figure 5a, black arrows). These HW splays occur where the main fault is observed to branch, partitioning the throw onto the two segments. These branching faults rapidly die out into the HW strata, with the majority of the throw remaining on the main TFZ segment, suggesting a breached relay zone. These splay faults can cause significant variations in the overall throw profile of the TFZ and may act to alter the sealing behaviour of the fault. Hence, the lack of splay faults intersecting the VFZ is unlikely to contribute significantly to the overall sealing potential of this fault.

#### 4.1.2 | Expansion index plots

The VFZ is interpreted to nucleate during the Permo-Triassic rifting event (Badley et al., 1988; Mulrooney et al., 2020). The fault then went through a period of tectonic quiescence lasting until the Late Jurassic (Sognefjord Formation). The fault was reactivated in the Late Jurassic (Draupne Formation) and continued to grow into the Late Cretaceous (Shetland Group). Only the northern-most section (3 km) of the fault shows reactivation in the Late Palaeocene (Sele Formation) (Figure 6a,b), indicating tip retreat. A similar growth history is recorded through EI plots for the TFZ. The only minor difference is that the TFZ does not show much, if any, reactivation in the Late Palaeocene (Sele Formation) (Figure 6c). Note that the apparent reactivation during the Late Jurassic–Cretaceous may be a product of the basin being sediment-starved during the Late Jurassic–Early Cretaceous, with subsequent significant sediment infill passively occurring in the Early Cretaceous by the Cromer Knoll Group (Bertram & Milton, 1988; Roberts et al., 2019).

Expansion indices of >1 within the lowermost growth strata (in this case the deepest mapped horizon is the Brent Group), occur at only a few hundred metres inward of the present lateral fault tip for both the VFZ and the TFZ (Figure 6b,d). This indicates that the fault had established its near-full length relatively early in the slip history before accumulating significant displacement, or that this is simply a product of reactivation of the Permo-Triassic fault, suggesting no further increase in fault length had occurred. Hence, this is consistent with the constant-length fault model. Note that only the southern fault tip is recorded for the VFZ due to the extent of the 3D survey.

#### 4.1.3 | Displacement backstripping

The length of the TFZ throughout backstripping is revealed to remain relatively constant, with no significant tip retreat observed (Figure 7, left). We can, therefore, hypothesise that the fault has grown by the constant-length model. This means that the length of the fault has established at an early stage, with no significant lateral fault growth, but subsequent displacement accumulation as the fault continued to grow. Increased fault segmentation is also observed through each backstripping increment, noted by the increased number of displacement minima along the length of the fault (Figure 7, left). This is especially prevalent within the Brent horizon at an early stage (when the displacement has been backstripped to the Sognefjord level).

Backstripping has also been performed for the VFZ. Note that no backstripping to the Shetland or Cromer Knoll could be performed, as the VFZ only penetrates these Groups at the northern-most end of the fault (roughly 7 km from the north) (see Mulrooney et al. (2020) for more details). The VFZ shows a slight tip retreat when backstripping is performed, where the fault had reached 87.5% of its final length early in its evolution. However, this is fairly minor, and in general, the length of the fault remains constant. Fault segmentation is observed to increase with both backstripping increments (Figure 7, right).

Note, however that a significant complication occurs during backstripping that needs to be considered. Despite showing a decrease in displacement towards either end of the fault, the precise location of the fault tip is not recorded on either end of the fault for the TFZ, and we have only recorded the tip for the southern-most end of the VFZ as our 3D seismic data does not cover the entirety of the VFZ. Hence, we can only use the displacement backstripping method as a best guess for the fault growth model that most accurately describes how these faults have grown. However, combining the results from displacement backstripping with EI plots will improve our confidence in their suggested fault growth history.

### 4.2 | Fault seal modelling

The TFZ is observed to fill to spill, associated with a high seal potential, likely through juxtaposition or a complete smear seal. If Troll East continued to fill, hydrocarbons should be discovered in well 31/6–3 due to the topography of the Sognefjord Formation (Figure 8f), and would probably be trapped by the continuation of the VFZ towards the South (see Wu et al., 2021 for details on the southern portion of the VFZ). However, no oil shows or gas readings were found within this well (https://factp

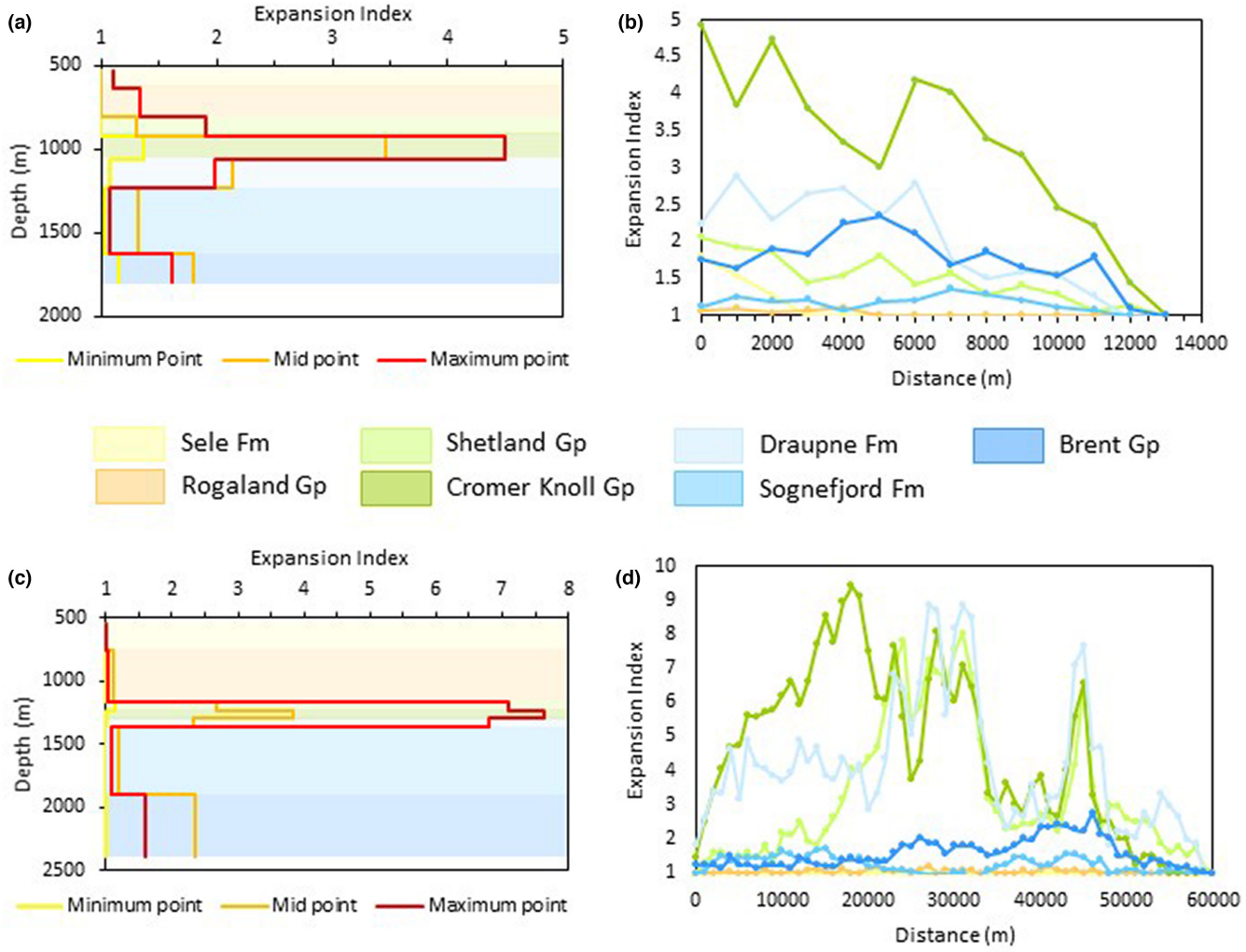


**FIGURE 6** Expansion Index (EI) plots for the Vette Fault Zone (VFZ) (a,b) and Tusse Fault Zone (TFZ) (c,d) shown. (a,c) EI plots with depth taken at the maximum throw, mid-point throw and minimum throw (near the fault tip). Depth location of the main horizons are coloured, shown in the key. (b,d) EI plotted against distance along the fault shown for each horizon, following the same colour key. Note that at the fault tips the EI values decrease to 1, or near to 1 for both faults.

ages.npd.no/en/wellbore/PageView/Exploration/All/35). Further, it might be suggested that hydrocarbon migration occurred into the FW of the VFZ through a relay zone at the southern extent of the GN1101 3D survey (see Mulrooney et al., 2020; Wu et al., 2021 for relay zone location and southern continuity of the VFZ). However, neither was there any evidence for hydrocarbon migration within well 32/4-3S within the Gladsheim prospect that occurs within the FW of the VFZ (Wu et al., 2021; https://factpages.npd.no/en/wellbore/pageview/exploration/all/8900; see Figure 1 for well location). Hence, we may hypothesise that the hydrocarbons had to migrate across the TFZ. Although it may be assumed the TFZ has a high seal potential through juxtaposition and/or smearing, the VShale is observed to be low within the juxtaposed Cromer Knoll and Shetland Group (Figures 3 and 8a). Hence, for completeness, to examine whether the hydrocarbon contact depth observed for Troll East is controlled by the fault membrane seal, fault seal analysis, specifically shale gouge ratio (SGR), has been calculated and subsequently calibrated to estimate the maximum hydrocarbon column height in the FW of the TFZ (Figure 8).

The Shetland and Cromer Knoll Groups are juxtaposed against the FW Sognefjord Formation along the length of the fault (Figure 8g–i). At locations of low Vshale overlaps where the HW Shetland and Cromer Knoll Groups

**FIGURE 7** Displacement backstripping throw–displacement (T-D) plots for the Tusse Fault Zone (TFZ) (left) and the Vette Fault Zone (VFZ) (right). Note that the Cromer Knoll and Shetland Groups are not displacement at the Southern end of the VFZ, hence displacement backstripping can only be done to the Draupne and Sognefjord Formations. Similarly, the Shetland Group is not displaced at the Southern end of the TFZ, hence displacement backstripping can only be done to the Cromer Knoll Group, Draupne and Sognefjord Formations.

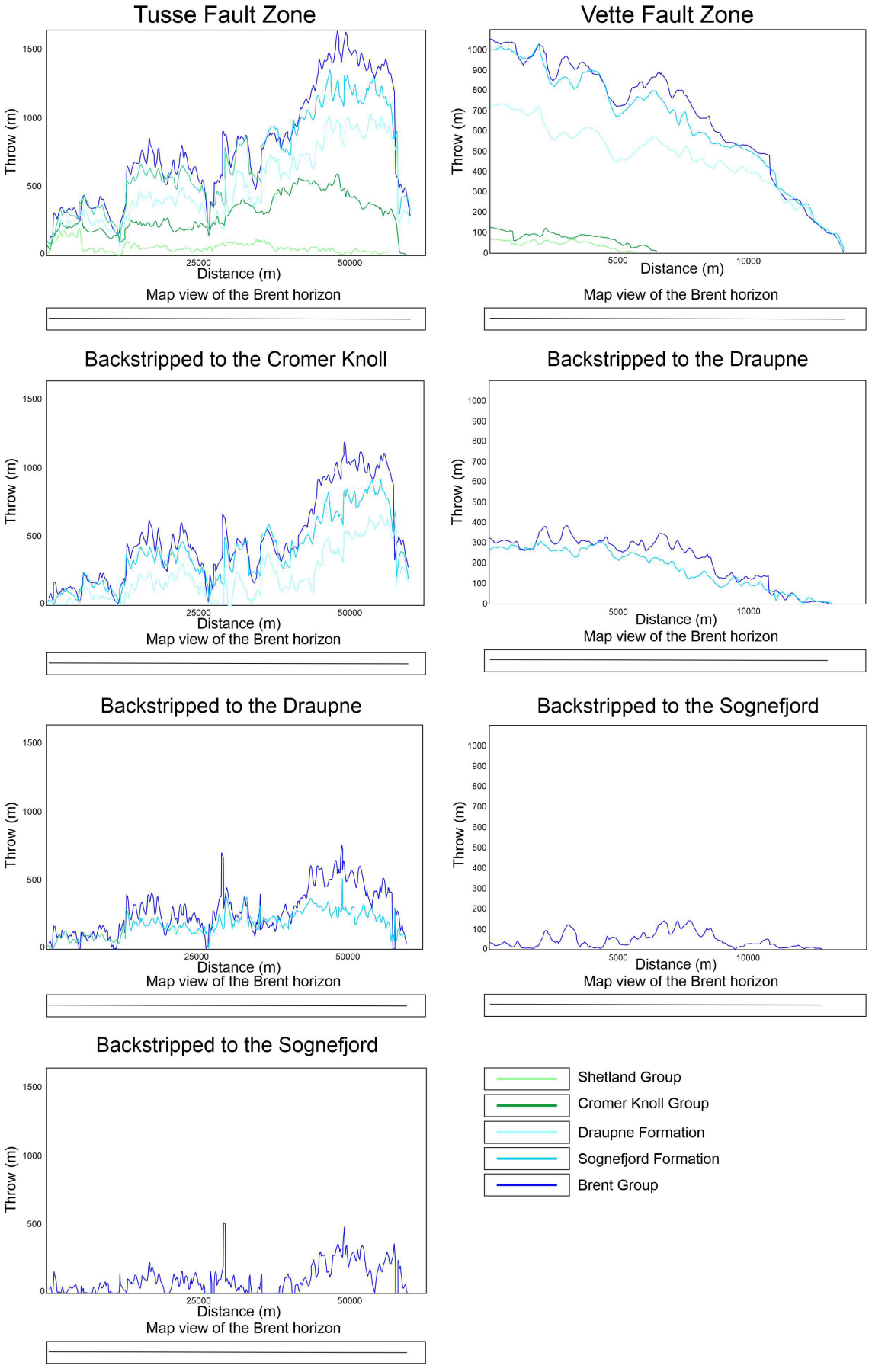

are juxtaposed the FW Sognefjord Formation (i.e. at interpreted sand–sand juxtapositions, where the VShale cut-off is set at 0.4), the SGR is calculated as being high (Figures 8a,b and 9b), with a minimum value of 26%, a maximum value of 72%, and an average value of 40%. The histogram of SGR for the TFZ shows the spread of SGR values calculated at low Vshale overlaps (Figure 9b).

Utilising the calculated SGR and more specifically the maximum column height predicted along the length and depth of this fault, we can identify the weakest point on the fault that is likely to act as the leak point for any across-fault fluid flow. This would, therefore, estimate the contact depth and hence the size of the field (Figure 8a–c, black arrow), which can be compared with the location of the extents of the known Troll Field (Figure 8a, blue arrow). The SGR values, with no values at or below 20% (i.e. when faults generally act as conduits rather than barriers to flow; Yielding, 2002), we could assume a high seal potential. However, under these circumstances, it would be predicted that the fault could withhold roughly only 39.7 m column, which is substantially lower than the gas column in place (219 m), and hence the extents of the predicted field would be substantially smaller (Figure 8d vs. e). In order for the fault to fill a column of 219 m, we have back-calculated the minimum SGR values that would be required. We first calculated the buoyancy pressure using the densities for gas and water (detailed in the methodology section), along with the known column height of 219 m:

$$\Delta P = \left(\rho_w - \rho_h\right)gh \tag{3}$$

where $\Delta P$ is the buoyancy force in Pascals, $\rho_w$ is the water density in kg/m$^3$, $\rho_h$ is the hydrocarbon density in kg/m$^3$, $g$ is the acceleration due to gravity (9.81 ms$^{-2}$) and $h$ is the known hydrocarbon column height in metres (Berg, 1975; Schowalter, 1979; Smith, 1966; Watts, 1987).

Using the buoyancy pressure results from Equation (3), we can then calculate the required SGR to support this pressure, using the equation from Yielding et al. (2010) (Equation 2 in section 3.2). With a calculated buoyancy pressure of 19.08 bars, we would require an SGR of over 100% to withhold the gas column recorded in Troll East, which is impossible to occur in nature. Since the maximum calculated SGR is recorded as 55%, we can conclude that other mechanisms than a sole gouge membrane is the driving force behind the sealing potential and leak point of this fault. For example, we may assume that a complete juxtaposition seal is required to withhold this large column, likely to be in combination with other processes such as shale/marl smearing and cataclasis.

## 5 | DISCUSSION

### 5.1 | Fault growth history of the Vette and Tusse Fault Zones

Utilising information from EI plots and displacement backstripping we can assess which model best describes the way in which the TFZ and VFZ have evolved. The EI plots for both faults suggest that the fault has grown following the constant-length model, where EI values of 1 are only observed near to the fault tips (cf. Jackson et al., 2017). Displacement backstripping also supports this model for the TFZ, where the modelled fault tip has not shown any regression. However, the slight regression observed for the VFZ may suggest that the fault evolved by a hybrid of both models; where the fault mostly grew by the constant-length model early in its evolution, after which the fault may then have somewhat grown laterally, linking up with a nearby fault to create the length of the fault trace observed today, following the propagation fault model. This hypothesis could be supported by current T-D plots: the location of the regressed fault tip (at 14 km from the north; Figure 7) lines up with an interpretation of a relict breached relay zone in the Sognefjord Formation (also at roughly 14 km from the north; Figure 5b). Note that this analysis cannot be used to analyse the early fault growth stage within the Permo-Triassic, due to this time-series information being poorly resolved. The difficulty with discriminating timing for fault interaction is a common challenge for this analysis (Nicol et al., 2020). Hence, we are limited to analysing the Late Jurassic reactivation event only.

**FIGURE 8** Shale gouge ratio (SGR) calculated along the fault length shown at low VShale (<0.4) overlaps, that is at sand–sand juxtapositions for the Tusse Fault Zone (TFZ). Black arrow shows where the predicted spill point would be along the TFZ. Blue arrow shows where the actual contact depth of the hydrocarbons in Troll East has been recorded. Black box shows the location of the detailed fault surface showing SGR (b) and predicted maximum hydrocarbon column height (c). (d) Predicted column in place (40 m) shown on a depth structure map of the Top Sognefjord Formation, showing the size of the predicted hydrocarbon accumulation. (e) Actual column in place (219 m of gas) shown on a depth structure map of the Top Sognefjord Formation, showing the size of the measured hydrocarbons in place. (f) Depth structure map of the top Sognefjord Formation showing where the hydrocarbons would spill to if continued migration into the Troll East field occurred, and if the TFZ was a complete seal. (g–i) Seismic sections taken along the TFZ showing displaced stratigraphy. Location of sections shown on figure A.

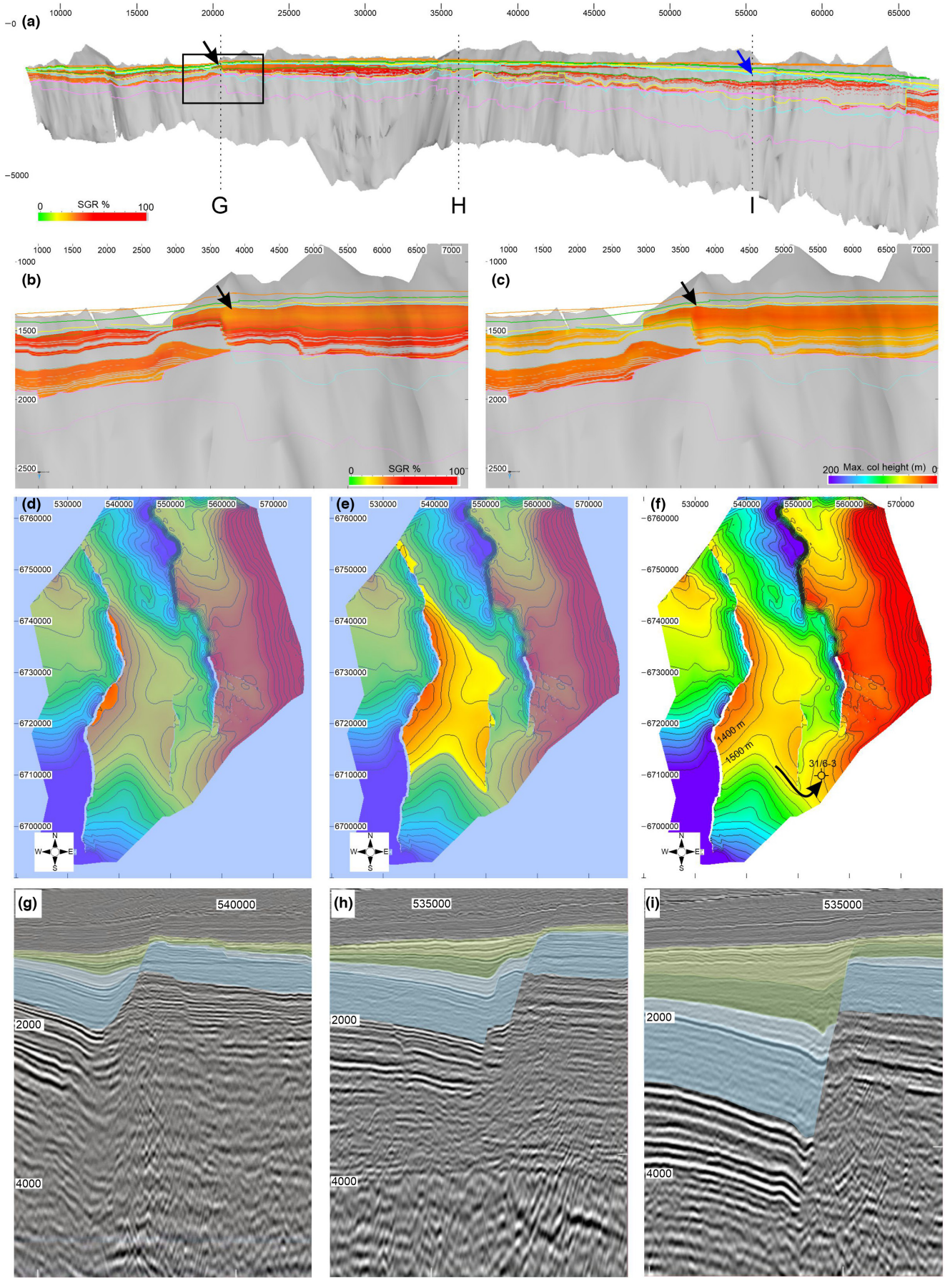

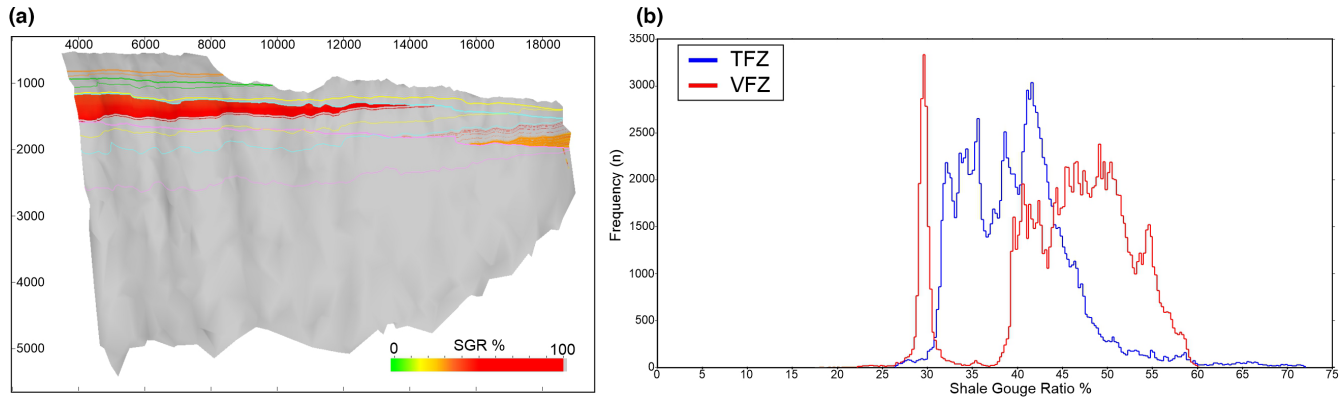


**FIGURE 9** (a) Shale gouge ratio (SGR) calculated along the fault length shown at low VShale (<0.4) overlaps, that is at sand–sand juxtapositions for the Vette Fault Zone (VFZ). (b) Histogram showing the frequency of SGR values for the Tusse Fault Zone (TFZ) (blue) and VFZ (red) at low VShale (<0.4) overlaps, where the Sognefjord Formation occurs within the Footwall.

The number of displacement minima along the length of the fault is observed to increase with each increment of backstripping (Figure 7), suggesting a decrease in fault segmentation through time. These throw minima may indicate where possible relict breached relays occurred during early fault development (Jackson et al., 2017), and as progressive displacement increase occurs, their presence may no longer observed using current T-D plots. Instead, those segments that are preserved on T-D plots show an increased amplitude and wavelength (see Figure 10a for description) when compared to the segments observed through backstripping. This may indicate that displacement accumulated along the fault in a non-uniform rate, consistent with the segmented history of the fault. Hence, this long fault is likely to have formed from multiple fault segments, favouring the propagation model early in the fault growth history (see Torabi et al., 2019). However, it is important to note that utilising this result for fault growth analysis should be used with caution, as the inferred increase in displacement minima may simply be a product of any irregularities in the younger horizons being superimposed on the older horizons if the relict breached relay zones do not line up vertically.

Examining T-D plots for the VFZ and TFZ we can see that the distribution and size of the relict breached relay zones vary along fault strike. In general, relay zones have been acknowledged as being potential pathways for fluid flow (Fossen & Rotevatn, 2016, and references therein), and have been shown to influence geothermal fluid activity (Curewitz & Karson, 1997) and migration of natural $CO_2$ (Dockrill & Shipton, 2010). Hence, to assess the impact, if any, of the relict breached relay zones on any possible fluid flow, we have quantified the geometry of the intersections using the throw amplitude variation and peak-to-peak wavelength (Figure 10a). Specifically, amplitude/wavelength was performed for both segments, with the results summed. This aggregation provides a proxy for the strains accommodated in the intersection zone for the two fault segments. We have then examined the size of the intersections in relation to the spill point of the Troll East Field for the TFZ, in order to assess whether the size of the intersecting zone may influence the seal potential of a fault. If we use the same assumptions made for the TFZ, this analysis may then be used as a predictive tool for any potential seep point along the VFZ (discussed in section 5.4). We can observe that the size of intersections is relatively small towards the northern end of the TFZ that is low amplitude/wavelength values (Figure 10b). The size of the relict breached relay zones increases subtly from north-to-south until roughly 53 km from the north, that is at fault intersection 16 (Figure 10d). The size of the amplitude/wavelength variation then increases dramatically. This increase in relict breached relay zone size correlates with the location of the southern limit to Troll East. We, therefore, hypothesise that one possible control on the extents of Troll East is relict breached relay(s) at this section of the fault, caused by increased fracturing that may have occurred during early evolution of relay zones (Bense & Van Balen, 2004; Childs et al., 1995; Peacock & Sanderson, 1994; Rotevatn et al., 2009; Trudgill & Cartwright, 1994). This hypothesis assumes that the increased fracturing is likely to remain as the relay zones evolved into breached relays, then relict breached relay zones. This is despite the fact that the fault likely developed rapidly in early fault growth history, quickly linking with other faults, and establishing its final length early in fault growth history. Furthermore, any variation in stratigraphic juxtaposition creating a weakness in the fault seal strength is unlikely, as the juxtaposing stratigraphy remains the same along the length of the TFZ; where the Shetland and Cromer Knoll Groups are consistently juxtaposed against the Sognefjord Formation (Figure 8g–i). However, no detailed lithofacies variation analysis has been performed.

Based on the size of the relict breached relay zones and how they relate to the spill point of Troll East, we propose an amplitude/wavelength ratio threshold size of 0.15. Above this value would be predicted the fault to act as a conduit, and below would have little/no influence on the seal capacity of the fault (Figure 10b,d). Relict breached relay zones with low amplitude/wavelengths are likely to have lower strain, accommodated by a lower density of deformation structures such as fractures. However, increased amplitude/wavelength overlap size is likely to correlate with an increased fracture density (Figure 10f). Furthermore, fault linkage can create intensely fractured lenses (Braathen et al., 2009; Childs et al., 2009; Fossen & Rotevatn, 2016), which then break down to fault rock (Childs et al., 2009). Increased fracturing may be inherited by the fault rock development to create a high permeability breccia lens.

It is important to note that the hypothesised cross-fault fluid flow potential is based on several assumptions. One major assumption is the deformation style that will occur within these fault zones. Clean sandstones, such as aeolian deposits will deform by mainly cataclasis at depth, creating lower permeability deformation bands (e.g. Antonellini & Aydin, 1994; Fisher & Knipe, 2001; Fossen et al., 2007, 2018; Torabi et al., 2013). These deformation bands require a high contrast with the surrounding host rock to have significant influence on fluid flow potential (Rotevatn et al., 2009; Torabi et al., 2013). However, the shallow burial depth at time of faulting, <1 km, would allow for the assumption that mainly disaggregation bands occurred, with granular flow in sand rather than cataclasis as the deformation mechanism (Wu et al., 2021), albeit there is significant uncertainty in depth versus style of deformation bands (e.g. Braathen et al., 2018). These disaggregation bands are unlikely to have significant influence on the fluid flow potential surrounding the faults (Rotevatn et al., 2009). Instead, fracturing within clean sandstones may also occur, as observed in other studies (e.g. Braathen et al., 2020; Davatzes & Aydin, 2003; Dockrill & Shipton, 2010; Ogata et al., 2014) and would be necessary to account for the potential spill point for Troll East, associated with a large relict breached relay zone acting as a fluid flow conduit. Cataclastic deformation, however, could account for additional column heights compared to SGR results (discussed below).

## 5.2 | Fault seal potential of the Tusse Fault Zone

The high calculated SGR values for the TFZ would only withhold an estimated column of roughly 40 m, with a leak point towards the northern end of the fault (Figure 8a,b black arrow, d), in comparison to the observed column height of 219 m, with a spill point significantly further to the south (Figure 8a blue arrow, e). Hence, another mechanism is needed to generate a higher seal capacity than the predicted gouge membrane. The SGR required to withhold the large gas column is >100%, suggesting a complete juxtaposition seal or continuous shale smear coupled with cataclastic processes as the key control for additional seal capacity (Nicol & Childs, 2018). The ductile behaviour of the shales could be evidenced by the drag folding observed within the hanging wall strata, associated with breaching of extensional monoclines related to the mechanically layered sequence (Ferrill et al., 2012; Jackson et al., 2006; Mulrooney et al., 2020). To assess the continuity of a shale smear, we use the Shale Smear Factor (SSF) algorithm. As detailed by Lindsay et al. (1993), the SSF is defined as:

$$\mathrm{SSF} = \frac{\text{Fault throw}}{\text{Shale layer thickness}} \tag{4}$$

Both outcrop and experimental shale smears suggest that smears become discontinuous at SSF >4–10 (e.g. Aydin & Eyal, 2002; Færseth, 2006; Lindsay et al., 1993; Takahashi, 2003). It has been noted that larger faults tend to display lower critical threshold values between continuous and discontinuous smears (Færseth, 2006). We can see for the TFZ, the minimum calculated SSF is 1.7, the maximum is >50, with a mean value of >50 (Figure 11a), which would lead to the conclusion of a discontinuous shale smear. Note that the Equation (4) largely defines smears from single shale beds, and hence does not take into consideration compound smearing involving two or more shale beds. However, as seen from the VShale logs in Figure 3, there are multiple shale beds in the overlying sequence, which may account for the surprisingly high SSF values. Furthermore, the high degree of heterogeneity within the juxtaposed Cromer Knoll and Shetland Groups, containing interbedded marls and limestones may account for areas with low VShale content, lowering the SGR and increasing the predicted SSF, but may in fact create wide zones of marl smearing, sealing the fault.

As a complementary approach to fault seal, we could consider fluid as migrating through cataclastic bands in the damage zones, degrading the flow at the fault. However, uncertainty exists as to their presence for our case (Wu et al., 2021). By applying Schueller et al.'s (2013) deformation band ratio versus throw, assigning an average 5-mm thickness to bands (Torabi & Fossen, 2009), and an average of 2.5 orders permeability reduction for bands compared to host rock (Ballas et al., 2015), we can gather rough values of deformation band properties that may hint at the impact on fluid flow. Using the Damage Zone width (W5 case) as a function of throw, as described by Schueller

et al. (2013), we can estimate a maximum damage zone width of roughly 63.5 m, given the maximum throw of 1335 m at the Sognefjord level. Using the same throw, we can estimate a maximum deformation band density of 12 bands/m (as described in Schueller et al., 2013), which will decrease logarithmically with distance from the fault. Based on the moderate burial depth, we can estimate a permeability reduction of 2.5 orders of magnitude (Ballas et al., 2015), which may create zones of permeability in the region of 3–26 mD. It is important to note that these areas of lower permeability will be distributed throughout the 64 m damage zone, and hence the bulk permeability will be greater. While these permeability values are unlikely to withhold a sizeable hydrocarbon column, they could act to impede flow at the fault, adding to the already high seal potential of these faults.

## 5.3 | Predicting the fault seal potential of the Vette Fault Zone using SGR, SSF and T-D plots

Using our knowledge of the possible fault seal potential of the TFZ, we can apply the same principles to the adjacent VFZ. For a fault to be considered as low risk to across-fault fluid flow, the fault should have low amplitude/wavelength values (<0.15) for any identified relict breached relay zones (Figure 12). Precise cut-off values for SGR and SSF cannot be provided due to the extraordinarily high seal strength of the TFZ that does not capture an SGR or SSF cut-off value. However, since the predicted SGR values have the ability to withhold a large column, we set a rough boundary of between 30 and 60% (Figure 12); that is the SGR values predicted for the TFZ (Figure 9). Furthermore, the low boundary of 30% SGR is generally stated as the cut-off value for faults to seal (Yielding et al., 2010). It is likely that the elevated SSF values for the TFZ is a product of the algorithm's inability to capture multiple shale beds in combination with the interbedded carbonates reducing the VShale value, when in fact any marl layers would add to the continuity of the shale smearing and further increase the seal strength. The SSF values for the VFZ are considerably lower (Figure 11b), potentially associated with the use of only one well for this analysis. We have kept the SSF cut-off value as varying about 4 (Lindsay et al., 1993; Figure 12). Areas highlighted in green on Figure 12 indicate a low risk to across-fault fluid flow. The fault may also show low risk where there are yellow areas; that is these are areas of uncertainty regarding the exact values used for SGR, SSF and amplitude/wavelength cut-offs (Figure 12). Specifically, ±10% has been added about the amplitude/wavelength 0.15 cut-off value, to allow for uncertainty. Areas shown in red are interpreted as high risk for across-fault fluid flow (Figure 12).

The predicted SGR for the VFZ is within similar bounds of the TFZ; the SGR at low VShale overlaps, where the Sognefjord Formation occurs within the FW, varies from 18 to 60%, with a mean average of 45%, compared with the TFZ with an SGR ranging from 26 to 72%, and an average value of 40% (Figure 9). Since we can assume that the SGR is not the sole contributing factor that influences the sealing potential for this fault, as mentioned above, we can suggest that the high seal potential is likely created by juxtaposition and smearing of low permeability layers from the overlying strata, specifically the shale and marl beds within the Cromer Knoll Group, potentially in combination with any cataclastic processes. We can see for the VFZ, the SSF calculated using Lindsay et al. (1993) shows a minimum value of 0.1, a maximum of >50, with a mean value of 12 (Figure 11c), but with the majority SSF values <5. Hence, it is likely the fault would show a continuous clay smear, sealing the fault to allow for a sizeable $CO_2$ accumulation within the Alpha prospect. We could, therefore, predict that the sealing potential of the VFZ is high, with low risk of across-fault fluid flow.

## 5.4 | Implications of fault growth analysis on $CO_2$ storage

As mentioned previously, one proposed explanation for the spill point for Troll East along the TFZ is at relict breached

**FIGURE 10** (a) Schematic throw–displacement (T-D) plot showing an interpreted fault–fault intersection location (identified by the vertical dashed line), where the geometry of this intersection is described by the throw amplitude for each segment (blue and green arrows), and the wavelength of the intersection (red arrow). The throw amplitude is identified using the peak-to-trough throw location for each of the intersecting segments. The throw wavelength is shown by the distance of the peak-to-peak location of the two intersecting segments. (b,c) amplitude/wavelength for the two fault segments, shown by intersection number for the Tusse Fault Zone (TFZ) and the Vette Fault Zone (VFZ), respectively. The intersection number is noted on Figure 5. The horizontal dashed line shows the amplitude/wavelength threshold value of 0.15. Points above this show potential to allow fluids to flow across or up the fault, whereas points below this threshold are likely to seal the fault. (d,e) T-D plots for the TFZ and VFZ, respectively, showing fault–fault intersections as vertical dashed lines, coloured whether these intersections may seal (green) or seep (red), using an amplitude/wavelength threshold value of 0.15. (f) Schematic diagrams showing how size of fault overlap may influence deformation structures. Increased strain may occur with increased amplitude/wavelength overlaps, leading to increased fracturing/deformation band density.

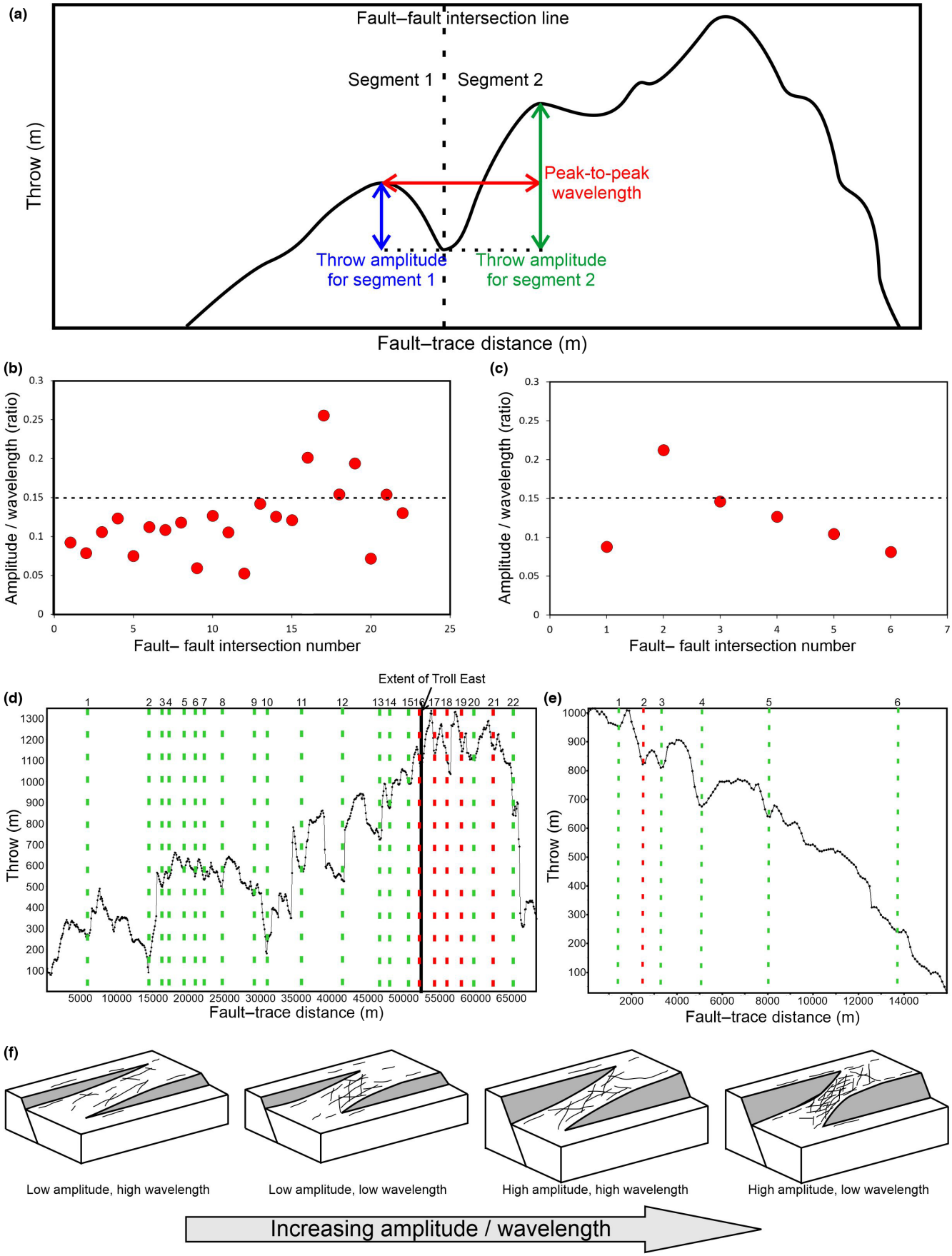

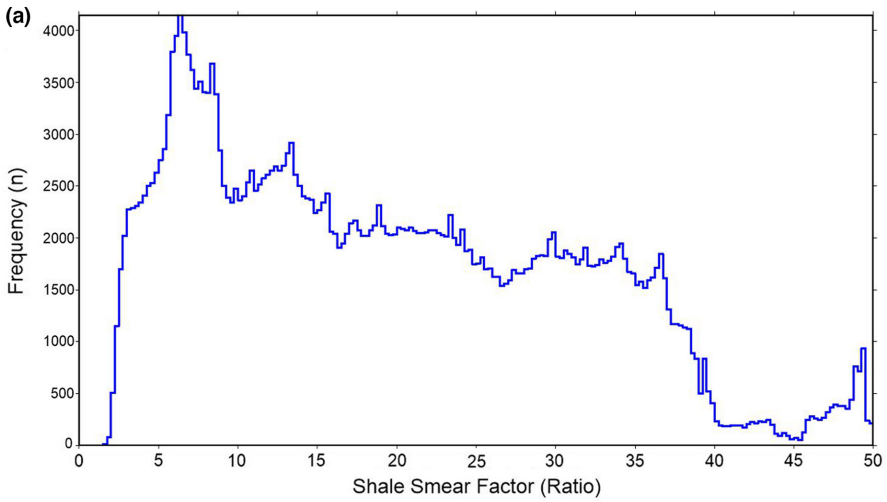


**FIGURE 11** Shale Smear Factor (SSF) histograms for the Tusse Fault Zone (TFZ) (a) and the Vette Fault Zone (VFZ) (b) where the Sognefjord Formation is observed in the Footwall. A large spread of SSF values occurs along the TFZ, with much narrower spread at lower values for the VFZ.

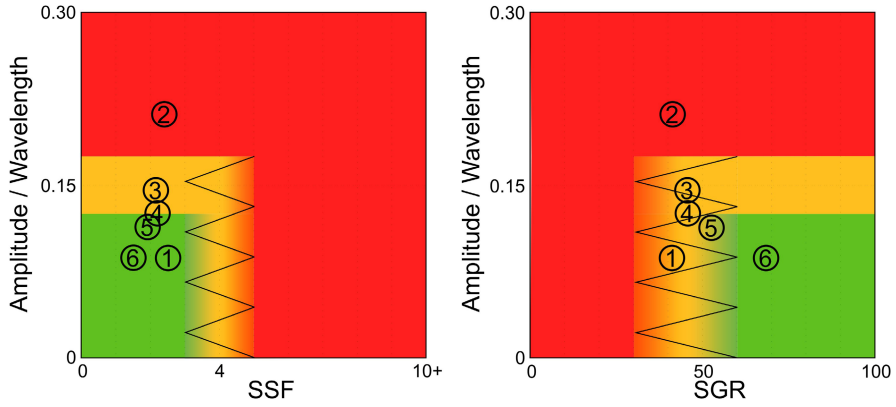


**FIGURE 12** Summary plots detailing scenarios when low risk (green) or high risk (red) faulting may occur. High risk is defined as a fault that has low SGR AND high SSF OR high amplitude/wavelength. Conversely, for a fault to be predicted as having a low risk, the fault is required to have a high SGR OR low SSF AND low amplitude/wavelength. The fault segments for the Vette Fault Zone (VFZ) (as identified and numbered in Figure 5) have been plotted on these summary plots.

relay zones that have a high amplitude/wavelength ratio (i.e. a large overlap between the two fault segments). Using the same amplitude/wavelength ratio threshold of 0.15 that is documented for the TFZ on the VFZ, in order to identify any possible high-risk areas along the fault, we can identify one relict breached relay zone that exceeds this threshold; intersection number 2, observed at roughly 2.5 km from the north, with an amplitude/wavelength value of 0.21 (Figures 10c,e and 12). Hence, we could propose that this could be an area of high risk for possible across-fault fluid flow and hence could cause seep of $CO_2$ injected into the Alpha prospect at Smeaheia, reducing

the volume of the storage site. However, there are two key differences between the fault segmentation of the TFZ and VFZ to increase uncertainty with this hypothesis: (i) the amplitude/wavelength of the relict breached relay zones on the TFZ reach higher values; and (ii) there are several large relict breach relay zones in close proximity to one another near the potential area of spill across the TFZ, which may all contribute to reducing the fault seal strength, rather than just one large relict breached relay zone causing across-fault fluid flow.

## 6 | SUMMARY

Analysing the sealing potential of the TFZ, we can predict that the fault is not sealed by a gouge membrane alone. Specifically, the calculated shale gouge ratio would not be high enough to withhold the measured 219 m gas column within the Troll East hydrocarbon Field. Instead, it is assumed that the fault's seal potential could be associated with a complete juxtaposition seal, shale/marl smearing in combination with cataclastic processes, generating an extremely high fault seal strength. Similarly, it is likely that the adjacent VFZ would also predict a high sealing potential. Hence, instead of high risk from a membrane seal breach, we hypothesise that the fault growth history will influence whether fluids can flow across- or up-fault.

The fault growth history for the TFZ, bounding the Troll East hydrocarbon Field, and the VFZ, bounding the Alpha prospect at the potential $CO_2$ storage site Smeaheia, both show a growth pattern predominantly following the constant-length growth model. This means that the faults have reached nearly their entire length early within the growth history, after which progressive displacement accumulation occurred. Utilising throw–distance plots, we can assess where any relict breached relay zones once occurred in the early stages of fault growth. The location and geometry of these intersections vary along the fault length. Where the geometry of these relict breached relay zones appears to be large, that is the amplitude/wavelength is greater than 0.15, we hypothesise that they may influence fluid flow across or up the fault. Specifically, the spill point for Troll East has been identified as coinciding with the first large (>0.15 amplitude/wavelength) relict breached relay zones from the north. Using the same hypothesis from the TFZ for the VFZ, we can identify one critical relict breached relay zone that may influence the ability of this fault to withhold a sizeable $CO_2$ column, rendering this fault a potential high risk.

### ACKNOWLEDGEMENTS

The authors acknowledge the following partners for their contributions: Aker Solutions, Ansaldo Energia, CoorsTek Membrane Sciences, EMGS, Equinor, Gassco, Krohne, Larvik Shipping, Lundin, Norcem, Norwegian Oil and Gas, Quad Geometrics, Total, Vår Energi, and the Research Council of Norway (RCN# 257579/E20). Badley Geoscience Ltd. are thanked for their academic licence of T7. Reviewers Graham Yielding and Andy Nicol are thanked for their thorough reviews that have improved the quality of the manuscript significantly.

### FUNDING INFORMATION

This is a contribution of the FRISK project, supported by the Research Council of Norway (RCN# 295061). Support from the NCCS Centre is acknowledged, performed under the Norwegian research program Centres for Environment-friendly Energy Research (FME).

### CONFLICT OF INTEREST STATEMENT

There is no conflict of interest.

### PEER REVIEW

The peer review history for this article is available at https://www.webofscience.com/api/gateway/wos/peer-review/10.1111/bre.12807.

### DATA AVAILABILITY STATEMENT

The data that support the findings of this study are available on request from the corresponding author. The data are not publicly available due to privacy or ethical restrictions.

### ORCID

*Emma Alexandra Harrower Michie* https://orcid.org/0000-0002-0488-2704

*Alvar Braathen* https://orcid.org/0000-0002-0869-249X

### REFERENCES

Allan, U. S. (1989). Model for hydrocarbon migration and entrapment within faulted structures. *AAPG Bulletin*, *73*(7), 803–811.

Antonellini, M., & Aydin, A. (1994). Effect of faulting on fluid flow in porous sandstones: Petrophysical properties. *AAPG Bulletin*, *78*(3), 355–377.

Aydin, A., & Eyal, Y. (2002). Anatomy of a normal fault with shale smear: Implications for fault seal. *AAPG Bulletin*, *86*(8), 1367–1381.

Badley, M. E., Price, J. D., Dahl, C. R., & Agdestein, T. (1988). The structural evolution of the northern Viking graben and its bearing upon extensional modes of basin formation. *Journal of the Geological Society*, *145*(3), 455–472.

Ballas, G., Fossen, H., & Soliva, R. (2015). Factors controlling permeability of cataclastic deformation bands and faults in porous sandstone reservoirs. *Journal of Structural Geology*, *76*, 1–21.

Barnett, J. A., Mortimer, J., Rippon, J. H., Walsh, J. J., & Watterson, J. (1987). Displacement geometry in the volume containing a single normal fault. *AAPG Bulletin*, *71*(8), 925–937.

Bell, R. E., Jackson, C. L., Elliott, G. M., Gawthorpe, R. L., Sharp, I. R., & Michelsen, L. (2014). Insights into the development of major rift-related unconformities from geologically constrained subsidence modelling: Halten terrace, offshore mid Norway. *Basin Research*, *26*(1), 203–224.

Bense, V. F., & Van Balen, R. (2004). The effect of fault relay and clay smearing on groundwater flow patterns in the lower Rhine embayment. *Basin Research*, *16*(3), 397–411.

Berg, R. R. (1975). Capillary pressures in stratigraphic traps. *AAPG Bulletin*, *59*(6), 939–956.

Bertram, G. T., & Milton, N. J. (1988). Reconstructing basin evolution from sedimentary thickness; the importance of palaeobathymetric control, with reference to the North Sea. *Basin Research*, *1*(4), 247–257.

Birol, F. (2008). *World energy outlook* (Vol. *23*, 329). International Energy Agency.

Braathen, A., Midtkandal, I., Mulrooney, M. J., Appleyard, T. R., Haile, B. G., & van Yperen, A. E. (2018). Growth-faults from delta collapse–structural and sedimentological investigation of the last chance delta, Ferron sandstone, Utah. *Basin Research*, *30*(4), 688–707.

Braathen, A., Petrie, E., Nystuen, T., Sundal, A., Skurtveit, E., Zuchuat, V., Gutierrez, M., & Midtkandal, I. (2020). Interaction of deformation bands and fractures during progressive strain in monocline-San Rafael swell, Central Utah, USA. *Journal of Structural Geology*, *141*, 104219.

Braathen, A., Tveranger, J., Fossen, H., Skar, T., Cardozo, N., Semshaug, S. E., Bastesen, E., & Sverdrup, E. (2009). Fault facies and its application to sandstone reservoirs. *AAPG Bulletin*, *93*(7), 891–917.

Bretan, P., Yielding, G., & Jones, H. (2003). Using calibrated shale gouge ratio to estimate hydrocarbon column heights. *AAPG Bulletin*, *87*(3), 397–413.

Cartwright, J., Bouroullec, R., James, D., & Johnson, H. (1998). Polycyclic motion history of some Gulf Coast growth faults from high-resolution displacement analysis. *Geology*, *26*(9), 819–822.

Cartwright, J. A., Mansfield, C., & Trudgill, B. (1996). The growth of normal faults by segment linkage. *Geological Society, London, Special Publications*, *99*(1), 163–177.

Cartwright, J. A., Trudgill, B. D., & Mansfield, C. S. (1995). Fault growth by segment linkage: An explanation for scatter in maximum displacement and trace length data from the canyonlands grabens of SE Utah. *Journal of Structural Geology*, *17*(9), 1319–1326.

Chapman, T.J. & Meneilly, A.W. (1991). *The displacement patterns associated with a reverse-reactivated, normal growth fault. Geological Society*, (Vol. *56,* pp. 183–191). Special Publications.

Childs, C., Holdsworth, R. E., Jackson, C. A. L., Manzocchi, T., Walsh, J. J., & Yielding, G. (2017). Introduction to the geometry and growth of normal faults. *Geological Society, London, Special Publications*, *439*(1), 1–9.

Childs, C., Manzocchi, T., Walsh, J.J., Bonson, C.G., Nicol, A. & Schöpfer, M.P. (2009). A geometric model of fault zone and fault rock thickness variations. *Journal of Structural Geology*, *31*(2), 117–127.

Childs, C., Watterson, J., & Walsh, J. J. (1995). Fault overlap zones within developing normal fault systems. *Journal of the Geological Society*, *152*(3), 535–549.

Cowie, P. A. (1998). A healing–reloading feedback control on the growth rate of seismogenic faults. *Journal of Structural Geology*, *20*(8), 1075–1087.

Cowie, P. A., & Scholz, C. H. (1992a). Displacement-length scaling relationship for faults: Data synthesis and discussion. *Journal of Structural Geology*, *14*(10), 1149–1156.

Cowie, P. A., & Scholz, C. H. (1992b). Physical explanation for displacement-length relationship of faults using a post-yield fracture mechanics model. *Journal of Structural Geology*, *14*, 1133–1148.

Curewitz, D., & Karson, J. A. (1997). Structural settings of hydrothermal outflow: Fracture permeability maintained by fault propagation and interaction. *Journal of Volcanology and Geothermal Research*, *79*(3–4), 149–168.

Davatzes, N. C., & Aydin, A. (2003). Overprinting faulting mechanisms in high porosity sandstones of SE Utah. *Journal of Structural Geology*, *25*(11), 1795–1813.

Dawers, N. H., & Anders, M. H. (1995). Displacement-length scaling and fault linkage. *Journal of Structural Geology*, *17*(5), 607–614.

Deng, C., Fossen, H., Gawthorpe, R. L., Rotevatn, A., Jackson, C. A., & FazliKhani, H. (2017). Influence of fault reactivation during multiphase rifting: The Oseberg area, northern North Sea rift. *Marine and Petroleum Geology*, *86*, 1252–1272.

Dockrill, B., & Shipton, Z. K. (2010). Structural controls on leakage from a natural $CO_2$ geologic storage site: Central Utah, USA. *Journal of Structural Geology*, *32*(11), 1768–1782.

Dreyer, T., Whitaker, M., Dexter, J., Flesche, H., Larsen, E. (2005). From spit system to tide dominated delta: integrated reservoir model of the upper Jurassic Sognefjord Formation on the Troll West Field. In: A.G. Doré, & B. Vining (Eds.), *Petroleum Geology of North-West Europe and Global Perspectives, Proceedings of the 6th Petroleum Geology Conference*. (pp. 1–26). Geological Society of London.

Duffy, O. B., Bell, R. E., Jackson, C. A. L., Gawthorpe, R. L., & Whipp, P. S. (2015). Fault growth and interactions in a multiphase rift fault network: Horda platform, Norwegian North Sea. *Journal of Structural Geology*, *80*, 99–119.

Færseth, R. B. (1996). Interaction of Permo-Triassic and Jurassic extensional fault-blocks during the development of the northern North Sea. *Journal of the Geological Society*, *153*(6), 931–944.

Færseth, R. B. (2006). Shale smear along large faults: Continuity of smear and the fault seal capacity. *Journal of the Geological Society*, *163*(5), 741–751.

Færseth, R. B., Gabrielsen, R. H., & Hurich, C. A. (1995). Influence of basement in structuring of the North Sea basin, offshore Southwest Norway. *Norsk Geologisk Tidsskrift*, *75*(2–3), 105–119.

Faleide, T. S., Braathen, A., Lecomte, I., Mulrooney, M. J., Midtkandal, I., Bugge, A. J., & Planke, S. (2021). Impacts of seismic resolution on fault interpretation: Insights from seismic modelling. *Tectonophysics*, *816*, 229008.

Ferrill, D. A., Morris, A. P., & McGinnis, R. N. (2012). Extensional fault-propagation folding in mechanically layered rocks: The case against the frictional drag mechanism. *Tectonophysics*, *576*, 78–85.

Fisher, Q. J., & Knipe, R. (1998). Fault sealing processes in siliciclastic sediments. *Geological Society, London, Special Publications*, *147*(1), 117–134.

Fisher, Q. J., & Knipe, R. J. (2001). The permeability of faults within siliciclastic petroleum reservoirs of the North Sea and Norwegian continental shelf. *Marine and Petroleum Geology*, *18*(10), 1063–1081.

Fossen, H., & Rotevatn, A. (2016). Fault linkage and relay structures in extensional settings—A review. *Earth-Science Reviews*, *154*, 14–28.

Fossen, H., Schultz, R. A., Shipton, Z. K., & Mair, K. (2007). Deformation bands in sandstone: A review. *Journal of the Geological Society*, *164*(4), 755–769.

Fossen, H., Soliva, R., Ballas, G., Trzaskos, B., Cavalcante, C., & Schultz, R. A. (2018). A review of deformation bands in reservoir sandstones: Geometries, mechanisms and distribution. *Geological Society, London, Special Publications*, *459*(1), 9–33.

Goldsmith, P. J. (2000), Exploration potential east of the Troll field, offshore Norway, after dry well 32/4-1, In K. Ofstad, J. E. Kittilsen, & P. Alexander-Marrack, (Eds.), *Improving the exploration process by learning from the past: Oslo, Norway*, (Vol. 9, pp. 65–97), Norwegian Petroleum Society Special Publication. https://doi.org/10.1016/S0928-8937(00)80010-7

Gradstein, F. M., & Waters, C. N. (2016). Stratigraphic guide to the Cromer Knoll, Shetland and chalk groups, North Sea and Norwegian Sea. *Newsletters on Stratigraphy*, *49*(1), 71–280.

Halland, E. K., Johansen, W. T., & Riis, F. (2011). *$CO_2$ storage atlas: Norwegian North Sea, Norwegian petroleum directorate*. http://www.npd.no/no/Publikasjoner/Rapporter/CO2-lagringsatlas

Holgate, N. E., Jackson, C. A. L., Hampson, G. J., & Dreyer, T. (2013). Sedimentology and sequence stratigraphy of the middle–upper jurassic krossfjord and fensfjord formations, troll field, northern North Sea. *Petroleum Geoscience*, *19*(3), 237–258.

Huggins, P., Watterson, J., Walsh, J. J., & Childs, C. (1995). Relay zone geometry and displacement transfer between normal faults recorded in coal-mine plans. *Journal of Structural Geology*, *17*(12), 1741–1755.

Isaksen, G. H., & Ledje, K. H. I. (2001). Source rock quality and hydrocarbon migration pathways within the greater Utsira high area, Viking graben, Norwegian North Sea. *AAPG Bulletin*, *85*(5), 861–883.

Jackson, C. A. L., Bell, R. E., Rotevatn, A., & Tvedt, A. B. (2017). Techniques to determine the kinematics of synsedimentary normal faults and implications for fault growth models. *Geological Society, London, Special Publications*, *439*(1), 187–217.

Jackson, C. A. L., & Rotevatn, A. (2013). 3D seismic analysis of the structure and evolution of a salt-influenced normal fault zone: A test of competing fault growth models. *Journal of Structural Geology*, *54*, 215–234.

Jackson, C. A. L., Gawthorpe, R. L., & Sharp, I. R. (2006). Style and sequence of deformation during extensional fault-propagation folding: Examples from the Hammam Faraun and El-Qaa fault blocks, Suez Rift, Egypt. *Journal of Structural Geology*, *28*(3), 519–535.

Justwan, H., Dahl, B. (2005). Quantitative hydrocarbon potential mapping and organo-facies study in the Greater Balder area, Norwegian North Sea. 2005. In: A.G. Dore, A. & Vinino, (Eds.), *Petroleum Geology*, (pp. 1317–1329). Northwest Europe and global prospective e Proceedings of the 6th Petroleum Geology Conference.

Karolytė, R., Johnson, G., Yielding, G., & Gilfillan, S. M. (2020). Fault seal modelling–the influence of fluid properties on fault sealing capacity in hydrocarbon and $CO_2$ systems. *Petroleum Geoscience*, *26*, 481–497.

Lauritsen, H., Kassold, S., Meneguolo, R., & Furre, A. (2018). Assessing potential influence of nearby hydrocarbon production on $CO_2$ storage at Smeaheia. In *Fifth $CO_2$ geological storage workshop* (Vol. *2018*, pp. 1–5). European Association of Geoscientists & Engineers.

Lewis, M. M., Jackson, C. A. L., & Gawthorpe, R. L. (2013). Salt-influenced normal fault growth and forced folding: The Stavanger fault system, North Sea. *Journal of Structural Geology*, *54*, 156–173.

Lindsay, N. G., Murphy, F. C., Walsh, J. J., & Watterson, J. (1993). Outcrop studies of shale smears on fault surfaces. In S. Flint & I. Bryant (Eds.), *The geological modelling of hydrocarbon reservoirs and outcrop analogues* (Vol. *15*, pp. 113–123). Blackwell Scientific Publications.

Lyon, P. J., Boult, P. J., Hillis, R. R., & Mildren, S. D. (2005). *Sealing by shale gouge and subsequent seal breach by reactivation: A case study of the Zema Prospect*. Otway Basin.

Michie, E. A., Alaei, B., & Braathen, A. (2022). Assessing the accuracy of fault interpretation using machine-learning techniques when risking faults for $CO_2$ storage site assessment. *Interpretation*, *10*(1), T73–T93.

Michie, E. A., Mulrooney, M. J., & Braathen, A. (2021). Fault interpretation uncertainties using seismic data, and the effects on fault seal analysis: A case study from the Horda platform, with implications for $CO_2$ storage. *Solid Earth*, *12*(6), 1259–1286.

Mondol, N. H., Fawad, M., & Park, J. (2018). Petrophysical analysis and rock physics diagnostics of Sognefjord formation in the Smeaheia area, northern North Sea. In *Fifth $CO_2$ geological storage workshop* (Vol. *2018*, pp. 1–5). European Association of Geoscientists & Engineers.

Morley, C. K., Nelson, R. A., Patton, T. L., & Munn, S. G. (1990). Transfer zones in the East African rift system and their relevance to hydrocarbon exploration in rifts. *AAPG Bulletin*, *74*(8), 1234–1253.

Mulrooney, M. J., Osmond, J. L., Skurtveit, E., Faleide, J. I., & Braathen, A. (2020). *Structural analysis of the Smeaheia fault block, a potential $CO_2$ storage site, northern Horda platform, North Sea*. Marine and Petroleum Geology. https://doi.org/10.1016/j.marpetgeo.2020.104598

Nicol, A., & Childs, C. (2018). Cataclasis and silt smear on normal faults in weakly lithified turbidites. *Journal of Structural Geology*, *117*, 44–57.

Nicol, A., Walsh, J., Berryman, K., & Nodder, S. (2005). Growth of a normal fault by the accumulation of slip over millions of years. *Journal of Structural Geology*, *27*(2), 327–342.

Nicol, A., Walsh, J., Childs, C., & Manzocchi, T. (2020). The growth of faults. In T. David & B. Christian (Eds.), *Understanding faults*. (pp. 221–255). Elsevier.

Nicol, A., Walsh, J. J., Villamor, P., Seebeck, H., & Berryman, K. R. (2010). Normal fault interactions, paleoearthquakes and growth in an active rift. *Journal of Structural Geology*, *32*(8), 1101–1113.

Nicol, A., Watterson, J., Walsh, J. J., & Childs, C. (1996). The shapes, major axis orientations and displacement patterns of fault surfaces. *Journal of Structural Geology*, *18*(2–3), 235–248.

Nybakken, S., & Bäckstrøm, S. A. (1989). Shetland group: Stratigraphic subdivision and regional correlation in the Norwegian North Sea. In J.D. Collinson (Ed.), *Correlation in hydrocarbon exploration* (pp. 253–269). Springer.

Ogata, K., Senger, K., Braathen, A., & Tveranger, J. (2014). Fracture corridors as seal-bypass systems in siliciclastic reservoir-cap rock successions: Field-based insights from the Jurassic entrada

formation (SE Utah, USA). *Journal of Structural Geology*, *66*, 162–187.

Osmond, J. L., Mulrooney, M. J., Holden, N., Skurtveit, E., Faleide, J. I., & Braathen, A. (2022). Structural traps and seals for expanding $CO_2$ storage in the northern Horda platform, North Sea. *AAPG Bulletin*, *106*(9), 1711–1752.

Patruno, S., Hampson, G. J., Jackson, C. A. L., & Whipp, P. S. (2015). Quantitative progradation dynamics and stratigraphic architecture of ancient shallow-marine clinoform sets: A new method and its application to the upper Jurassic Sognefjord formation, troll field, offshore Norway. *Basin Research*, *27*(4), 412–452.

Peacock, D. C. P., & Sanderson, D. J. (1991). Displacements, segment linkage and relay ramps in normal fault zones. *Journal of Structural Geology*, *13*(6), 721–733.

Peacock, D. C. P., & Sanderson, D. J. (1994). Geometry and development of relay ramps in normal fault systems. *AAPG Bulletin*, *78*(2), 147–165.

Petersen, K., Clausen, O. R., & Korstgård, J. A. (1992). Evolution of a salt-related listric growth fault near the D-1 well, block 5605, Danish North Sea: Displacement history and salt kinematics. *Journal of Structural Geology*, *14*(5), 565–577.

Rider, M. (2000). *The geological interpretation of well logs* (second ed., pp. 126–128). Rider–French Consulting Ltd.

Ringrose, P. S., Thorsen, R., Zweigel, P., Nazarian, B., Furre, A. K., Paasch, B., Thompson, N., & Karstad, P. I. (2017). Ranking and risking alternative $CO_2$ storage sites offshore Norway. In *Fourth sustainable earth sciences conference* (Vol. *2017*, pp. 1–5). European Association of Geoscientists & Engineers.

Rippon, J. H. (1984). Contoured patterns of the throw and hade of normal faults in the coal measures (Westphalian) of north-east Derbyshire. *Proceedings of the Yorkshire Geological Society*, *45*(3), 147–161.

Roberts, A. M., Kusznir, N. J., Yielding, G., & Beeley, H. (2019). Mapping the bathymetric evolution of the northern North Sea: From Jurassic synrift archipelago through cretaceous–tertiary post-rift subsidence. *Petroleum Geoscience*, *25*(3), 306–321.

Rogelj, J., Den Elzen, M., Höhne, N., Fransen, T., Fekete, H., Winkler, H., Schaeffer, R., Sha, F., Riahi, K., & Meinshausen, M. (2016). Paris agreement climate proposals need a boost to keep warming well below 2°C. *Nature*, *534*(7609), 631–639.

Rotevatn, A., Fossen, H., Hesthammer, J., Aas, T. E., & Howell, J. A. (2007). Are relay ramps conduits for fluid flow? Structural analysis of a relay ramp in arches National Park, Utah. *Geological Society, London, Special Publications*, *270*(1), 55–71.

Rotevatn, A., Jackson, C. A. L., Tvedt, A. B., Bell, R. E., & Blækkan, I. (2019). How do normal faults grow? *Journal of Structural Geology*, *125*, 174–184.

Rotevatn, A., Kristensen, T. B., Ksienzyk, A. K., Wemmer, K., Henstra, G. A., Midtkandal, I., Grundvåg, S. A., & Andresen, A. (2018). Structural inheritance and rapid rift-length establishment in a multiphase rift: The East Greenland rift system and its Caledonian orogenic ancestry. *Tectonics*, *37*(6), 1858–1875.

Rotevatn, A., Tveranger, J., Howell, J. A., & Fossen, H. (2009). Dynamic investigation of the effect of a relay ramp on simulated fluid flow: Geocellular modelling of the delicate arch ramp, Utah. *Petroleum Geoscience*, *15*(1), 45–58.

Schlische, R. W. (1995). Geometry and origin of fault-related folds in extensional settings. *AAPG Bulletin*, *79*(11), 1661–1678.

Schowalter, T. T. (1979). Mechanics of secondary hydrocarbon migration and entrapment. *AAPG Bulletin*, *63*(5), 723–760.

Schueller, S., Braathen, A., Fossen, H., & Tveranger, J. (2013). Spatial distribution of deformation bands in damage zones of extensional faults in porous sandstones: Statistical analysis of field data. *Journal of Structural Geology*, *52*, 148–162.

Serck, C. S., & Braathen, A. (2019). Extensional fault and fold growth: Impact on accommodation evolution and sedimentary infill. *Basin Research*, *31*(5), 967–990.

Shipton, Z. K., Evans, J. P., & Thompson, L. B. (2005). The geometry and thickness of deformation-band fault core and its influence on sealing characteristics of deformation-band fault zones.

Smith, D. A. (1966). Theoretical considerations of sealing and non-sealing faults. *AAPG Bulletin*, *50*(2), 363–374.

Sperrevik, S., Gillespie, P. A., Fisher, Q. J., Halvorsen, T., & Knipe, R. J. (2002). Empirical estimation of fault rock properties. In G. Koestler Andreas, & R. Hunsdale (Eds.), *Norwegian petroleum society special publications* (Vol. *11*, pp. 109–125). Elsevier.

Statoil. (2016). Subsurface Evaluation of Smeaheia as part of 2016 Feasibility study on $CO_2$ storage in the Norwegian Continental Shelf. OED 15/1785. Document A–Underground report Smeaheia (Internal Report–Available on Request Only).

Sundal, A., Hellevang, H., Miri, R., Dypvik, H., Nystuen, J. P., & Aagaard, P. (2014). Variations in mineralization potential for $CO_2$ related to sedimentary facies and burial depth–a comparative study from the North Sea. *Energy Procedia*, *63*, 5063–5070.

Takahashi, M. (2003). Permeability change during experimental fault smearing. *Journal of Geophysical Research: Solid Earth*, *108*(B5).

Thorsen, C. E. (1963). Age of growth faulting in Southeast Louisiana. *Gulf Coast Association of Geological Societies Transactions*, *13*, 103–110.

Torabi, A., Alaei, B., & Libak, A. (2019). Normal fault 3D geometry and displacement revisited: Insights from faults in the Norwegian Barents Sea. *Marine and Petroleum Geology*, *99*, 135–155.

Torabi, A., & Fossen, H. (2009). Spatial variation of microstructure and petrophysical properties along deformation bands in reservoir sandstones. *AAPG Bulletin*, *93*(7), 919–938.

Torabi, A., Fossen, H., & Braathen, A. (2013). Insight into petrophysical properties of deformed sandstone reservoirs. *AAPG Bulletin*, *97*(4), 619–637.

Trudgill, B., & Cartwright, J. (1994). Relay-ramp forms and normal-fault linkages, canyonlands National Park, Utah. *Geological Society of America Bulletin*, *106*(9), 1143–1157.

Walsh, J. J., Bailey, W. R., Childs, C., Nicol, A., & Bonson, C. G. (2003). Formation of segmented normal faults: A 3-D perspective. *Journal of Structural Geology*, *25*(8), 1251–1262.

Walsh, J. J., Nicol, A., & Childs, C. (2002). An alternative model for the growth of faults. *Journal of Structural Geology*, *24*(11), 1669–1675.

Walsh, J. J., & Watterson, J. (1988). Analysis of the relationship between displacements and dimensions of faults. *Journal of Structural Geology*, *10*(3), 239–247.

Walsh, J. J., & Watterson, J. (1991). Geometric and kinematic coherence and scale effects in normal fault systems. *Geological Society, London, Special Publications*, *56*(1), 193–203.

Walsh, J. J., Watterson, J., Childs, C., & Nicol, A. (1996). Ductile strain effects in the analysis of seismic interpretations of normal fault systems. *Geological Society, London, Special Publications*, *99*(1), 27–40.

Watts, N. L. (1987). Theoretical aspects of cap-rock and fault seals for single-and two-phase hydrocarbon columns. *Marine and Petroleum Geology*, *4*(4), 274–307.

Whipp, P. S., Jackson, C. L., Gawthorpe, R. L., Dreyer, T., & Quinn, D. (2014). Normal fault array evolution above a reactivated rift fabric; a subsurface example from the northern Horda platform, Norwegian North Sea. *Basin Research*, *26*(4), 523–549.

Wu, L., Thorsen, R., Ottesen, S., Meneguolo, R., Hartvedt, K., Ringrose, P., & Nazarian, B. (2021). Significance of fault seal in assessing $CO_2$ storage capacity and containment risks—An example from the Horda platform, northern North Sea. *Petroleum Geoscience*, *27*. https://doi.org/10.1144/petgeo2020-102

Yielding, G. (2002). Shale gouge ratio—Calibration by geohistory. In G. Koestler Andreas, & R. Hunsdale (Eds.), *Norwegian petroleum society special publications* (Vol. *11*, pp. 1–15). Elsevier.

Yielding, G., Badley, M. E., & Freeman, B. (1991). Seismic reflections from normal faults in the northern North Sea. *Geological Society, London, Special Publications*, *56*(1), 79–89.

Yielding, G., Bretan, P., & Freeman, B. (2010). Fault seal calibration: A brief review. *Geological Society, London, Special Publications*, *347*(1), 243–255.

Yielding, G., Freeman, B., & Needham, D. T. (1997). Quantitative fault seal prediction. *AAPG Bulletin*, *81*(6), 897–917.

**How to cite this article:** Michie, E. A. H., & Braathen, A. (2024). How displacement analysis may aid fault risking strategies for $CO_2$ storage. *Basin Research*, *36*, e12807. https://doi.org/10.1111/bre.12807